2008

Active and passive microwave radiometry for transcutaneous measurements of temperature and oxygen saturation

Thomas A. Ricard
University of South Florida

Active and Passive Microwave Radiometry for Transcutaneous Measurements of Temperature and Oxygen Saturation

by

Thomas A. Ricard

A dissertation in partial fulfillment
of the requirements for the degree of
Doctor of Philosophy
Department of Electrical Engineering
College of Engineering
University of South Florida

Co-Major Professor: Thomas Weller, Ph.D.
Co-Major Professor: Jeffrey J. Harrow, M.D.
Shekhar Bhansali, Ph.D.
Lawrence Dunleavy, Ph.D.
Nagarajan Ranganathan, Ph.D.
John Whitaker, Ph.D.

Date of Approval:
July 18, 2008

Keywords: bioengineering, bioelectromagnetics, oxygen resonance, skin cancer, radiometric thermometry

Dedication

When I left my industry position in Connecticut and relocated to Florida in order to resume my formal education, I was far from the only person who was affected by that decision. I would like to dedicate this work to those persons closest to me who rearranged their lives so that I could be where I am today: my parents, Jean and Armand Ricard, my wife, Gina Harris Ricard and my daughters, Bernadette Allison and Amanda Valentine Ricard.

Acknowledgments

If it takes a village to raise a child, it certainly takes a small community to produce a dissertation. I am grateful to the following persons whose assistance and advice proved invaluable during my research and the preparation of this work:

My dissertation committee, especially Drs. Thomas Weller and Jeffrey Harrow.

Ms. Gina Ricard B.S. RRT – NPS, Hillsborough Community College, Tampa

Mr. Bernard Batson, IGERT and Bridge to Doctorate Programs, USF

Mr. Robert Roeder, Raytheon Company

Dr. Sanjukta Bhanja, Department of Electrical Engineering, USF

Dr. Joel Strom, Professor of Internal Medicine, USF

Dr. Neil Fenske, Department of Dermatology, USF

Ms. Karin Banach, Department of Dermatology, USF

Funding for my studies and research were provided in part by the NSF IGERT grant number DGE-0221681, by a grant from the Skin Cancer Foundation and by the Raytheon Company.

Table of Contents

List of Tables

List of Figures

Active and Passive Microwave Radiometry for Transcutaneous Measurements of Temperature and Oxygen Saturation

Thomas A. Ricard

ABSTRACT

In this work we explore two novel uses of microwave technology in biomedical applications. Introductory material on the electrical properties of biological tissues is presented to form the groundwork for the basic theory behind both techniques.

First, we develop a technique that uses 60 GHz signals to detect changes in blood oxidation levels. Several atmospheric propagation models are adapted to predict oxygen resonance spectra near this frequency. We are able to predict and observe the changes in these levels as the blood ages up to 48 hours. Identical testing procedures performed using arterial blood gas (ABG) calibration samples with controlled oxygen levels show similar results to those obtained as bovine blood ages. We then discuss a potential application of this technique to the detection and diagnosis of skin cancer.

The second application involves non-invasive measurement of internal body temperatures. Conventional methods of body temperature measurement provide a numerical value for a specific location on the body. This value is then applied to the

remaining body systems as a whole. For example, a measurement of 37° C obtained orally can possibly lead to the erroneous conclusion that temperature is normal throughout the body. Temperature measurements made on specific internal organs can yield more information about the condition of the body, and can be invaluable as a tool for performing remote diagnostic evaluations. We explore the use of microwave radiometry in the low GHz spectrum to show that temperature information can be obtained directly and non-invasively for internal organs. We use the principles of black-body radiation theory combined with the reflection and transmission characteristics of biological tissues to predict the temperature delta that would be externally measured, given specific changes in the internal temperature. Data taken using a microwave radiometer and planar structures made with biological phantoms are compared to analytical results, showing that detection of internal temperature changes of can be performed externally in this manner.

Chapter 1

Introduction

The form and function of the human body have been studied for millennia, using a variety of methods and technologies as they were adapted and became available. Some of these methods have included visual, chemical, mechanical and, more recently, radiological and computational techniques. The field of microwave engineering, having been refined in the mid-to-late 20^{th} century, remains a relatively undeveloped tool for the study of the body's surface and internal characteristics. In this work, we present the analysis and results of several potential implementations of the use of microwave signals to sense changes and abnormalities in and under the skin.

The techniques we will explore are microwave spectroscopy and microwave radiometry. The study of spectroscopy in this work is directed toward the detection of oxygen resonance lines by examining the signal reflection characteristics of oxygenated blood at frequencies around 60 GHz. While the study of oxygen resonances has a long and rich history in relation to communications and radar engineering [1]–[3], we are unaware of any previous effort to apply this phenomenon to the study of blood. Similarly, work has been performed only recently in characterizing the resonant frequencies of blood near 60 GHz [4].

Signal reflection generally occurs at points of change in the impedance presented to the signal during propagation. Typically, these changes are due to material properties in the propagation path or to changes in the structure in which propagation is taking place. In the biomedical field, changes in structure cannot always be accurately characterized; consequently, we will focus on the properties of the materials through which the signal is propagating.

Signal reflection is quantified by the unitless reflection coefficient Γ, which is defined in terms of the material intrinsic impedance η by [5]

$$\Gamma = \frac{\eta - \eta_0}{\eta + \eta_0} \quad , \tag{1-1}$$

where η_0 indicates the intrinsic impedance of the original material through which the wave is propagating and η is the impedance of a different material on the other side of a boundary. Since the complex value of the intrinsic impedance η is dependent on the complex material permittivity ε, we devote a large portion of Chapter 2 to the subject of permittivity and its uses in material characterizations and analysis.

Assuming that η (and η_0) are constant with frequency (which is a reasonable assumption for small bandwidths), we would expect Γ to likewise remain constant with frequency. However, the reflection coefficient decreases considerably at resonant

frequencies, not directly due to changes in material impedances, but to quantum energy changes at the molecular level [6], [7].

Chapter 3 is devoted to the study of this resonance phenomenon in oxygenated blood. We show that changes in signal reflection characteristics are related to those documented in atmospheric propagation studies, and can be detected for small volumes of material. The primary motivation for this area of research is the early detection of skin cancer. While conventional techniques such as excision and biopsy are quite effective in determining the presence of malignant activity, this approach is not without its drawbacks. For example, excision is invasive by nature, and as such can be a source of intimidation to some patients. Time is also a factor, since the excised material must be examined *in vitro*, often at a different location from the patient, to obtain a diagnosis. Cost can be a major problem for those patients without health insurance coverage. The technology developed in this work may provide a means to non-invasively produce immediate results at little or no cost to the patient.

Chapter 4 deals with microwave radiometry, which is based on the principle of blackbody radiation: the phenomenon of all objects with a non-zero absolute temperature to emit RF energy. Emission of this energy occurs at very low signal levels over an extremely wide frequency range, with the peak amplitude and frequency of blackbody emission dependent on the absolute temperature of the object [8], [9].

In Chapter 4 we investigate the implementation of radiometry to the measurement of internal body temperatures; specifically, the temperatures of vital organs and tissues of astronauts during extended missions in space. In order to analyze a multi-layered structure to determine the characteristics of an internal layer, we must take into account such factors as material propagation and impedance and multiple boundary reflection coefficients. Transmission and reflection phase characteristics must also be considered if an accurate coherent model is to be achieved.

We show the results of a first approximation analysis and compare those to data collected using a simple 1.4 GHz radiometer. The test structure consists of planar layers of biological phantoms that have similar electrical properties to those of muscle, fat and skin tissues.

1.1 Organization and Contributions

We begin in Chapter 2 by introducing key concepts that describe interaction between microwaves and materials, and characteristic values for common tissues.

Chapter 3 is devoted to the detection of tissue oxygenation by the means of sensing oxygen resonances in the microwave frequency range. In this chapter we present the results of several resonance approximation techniques and show measurements confirming the validity of the basic theory. In presenting this information, we demonstrate the basic technique of a real-time, noninvasive method for determining

tissue oxygenation. The primary motivation for this study is the detection of malignant activity on and just below the skin, but other applications, such as the studies of psoriasis and burn and wound healing are discussed.

Chapter 4 presents an application of microwave radiometry. The technique is applied to the detection and quantification of internal organ temperature changes. After a brief review of radiometric theory and principles, we show the results of analyses of simple planar structures and the correlation of these results with the measurements made using a microwave frequency radiometer. This study was initiated as part of a space suit design for astronauts on extended journeys, and as such has great potential toward the advancement of space exploration and future human colonization of other planets. This technique also has potential applications in the fields of surgery, critical health monitoring, and fire detection.

It is our hope that this material may provide some new directions for the use of microwave techniques in biological and medical applications, and may ultimately serve toward a betterment of the human condition.

Chapter 2

Electrical and RF Properties of Biological Materials

In this chapter we will review some of the basic mechanisms of the interactions between radio frequency (RF) and microwave energy and biological tissues and materials. Those interactions with which we will be concerned include the effect of skin and subcutaneous materials on the propagation characteristics of microwave signals. In order to ensure a thorough presentation of the properties that affect signal propagation within the body, we must begin with a review of complex permittivity and show how other properties, such as conductivity, attenuation and impedance can be derived from this quantity. Information that is specific to a particular technique is presented in later chapters, that is, spectrographic and radiometric material will be relegated to Chapters 3 and 4, respectively.

2.1 Properties Database

Much of the numerical information presented in this work is derived from the data and formulas contained in Compilation of the Dielectric Properties of Body Tissues at RF and Microwave Frequencies, compiled by Gabriel and Gabriel for King's College in London [10]. One intent of this report was "…to derive models for the frequency

dependence of the dielectric properties of the tissues investigated…". The report presents the parameters for and uses a four-term Cole-Cole model [11] to account for the dispersion levels found in wide-band frequency studies of biological material behavior. Forty-four types of material are characterized in this report, including body fluids, tissues and organs.

Computation of the material characteristics can be accomplished by any number of means. However, a ready-made implementation of the Gabriel model is available: the "Tissue Dielectric Properties Calculator" spreadsheet by Anderson and Rowley for Telstra Research Laboratories [12]. This spreadsheet provides rapid evaluation of the Gabriel model over the frequency range of 10 Hz to 100 GHz, and was used to obtain the data for many of the tissue characteristics plots in this work. Plots corresponding to representative biological materials are included as part of the development in this chapter; more are contained in Appendix A.

2.2 Complex Permittivity

Any discussion of the interaction of RF and microwave fields with biological materials and tissues must take into account the constitutive parameters of these materials. As discussed in [13], these parameters include electric permittivity ε in Farads per meter (F/m), magnetic permeability μ in Henries per meter (H/m), and conductivity σ in Siemens per meter (S/m).

Permittivity and permeability are represented as complex quantities as follows:

$$\varepsilon = \varepsilon' - j\varepsilon'', \tag{2-1}$$

and

$$\mu = \mu' - j\mu'', \tag{2-2}$$

respectively.

Since the human body is considered to be nonmagnetic and transparent to magnetic fields [14], the behavior of magnetic fields and their effect on biological materials and processes need not be considered here. Consequently, we can assume a scalar value of 1 for the relative permeability of any materials under discussion, and use the free-space permeability (μ_0) value of $4\pi \times 10^{-7}$ H/m wherever permeability forms part of a relationship.

The permittivity value ε is a product of the complex relative permittivity ε_r and the permittivity of free space ($\varepsilon_0 \approx 8.8542 \times 10^{-12}$ F/m). Thus,

$$\varepsilon = \varepsilon_0 \varepsilon_r , \tag{2-3}$$

or, in complex notation,

$$\varepsilon' - j\varepsilon'' = \varepsilon_0(\varepsilon_r' - j\varepsilon_r'') . \tag{2-4}$$

The relationship between the real and imaginary components of the complex permittivity is often referred to as the loss tangent and is expressed as

$$\tan \theta = \varepsilon_r'' / \varepsilon_r' . \tag{2-5}$$

In materials in which ε_r'' is a function of frequency, the value of this function reaches a local maximum at a frequency f corresponding to a relaxation time τ, where the relationship between frequency and time is defined by

$$\tau \text{ (seconds)} = 1/(2\pi f) \text{ (Hertz)} . \tag{2-6}$$

It has been shown [15] that ε_r' is a function of frequency if ε_r'' is non-zero at any point in the frequency domain. If ε_r'' reaches a single maximum value as a function of frequency, then the real and imaginary components of the complex permittivity can be approximated by a first order Debye equation, expressed as

$$\varepsilon_r' = \frac{\varepsilon_{r0} - \varepsilon_{r\infty}}{1 + \omega^2 \tau^2} + \varepsilon_{r\infty} \tag{2-7}$$

and

$$\varepsilon_r'' = \frac{(\varepsilon_{r0} - \varepsilon_{r\infty})\omega\tau}{1 + \omega^2 \tau^2} \quad , \tag{2-8}$$

respectively, where

$\omega = 2\pi f$ is the radian frequency,

ε_{r0} is the relative permittivity at zero frequency, and

$\varepsilon_{r\infty}$ is the relative permittivity at infinite frequency (also called the optical dielectric constant) [15].

Since biological tissues and materials have constitutive parameters that exhibit generally non-linear behavior as a function of frequency, more relaxation times (and consequently, higher-order equations) are needed in order to model the frequency dependence of permittivity with reasonable accuracy. The analyses contained in this work are based on a fourth order Cole-Cole expression for permittivity, which is

$$\varepsilon(\omega) = \varepsilon_0 + \sum_{m=1}^{4} \frac{\Delta\varepsilon_m}{1 + j\omega\tau_m^{(1-\alpha_m)}} + \sigma / j\omega\varepsilon_0 \ , \tag{2-9}$$

where

$\Delta\varepsilon_m$ is the value of the frequency-dependent change in permittivity,

τ_m is the corresponding relaxation time,

α_m is a fitting parameter, and

σ represents ionic conductivity [10].

The values of each of the parameters in equation (2-9) are shown in Table 2-1 for various biological materials.

Table 2-1

Four Term Cole-Cole Parameters for Select Biological Materials

(Adapted from [10])

Tissue	ε_∞	$\Delta\varepsilon_1$	τ_1	α_1	$\Delta\varepsilon_2$	τ_2	α_2
Blood	4.000	40.00	8.842	0.100	50	3.183	0.100
Dry Skin	4.000	32.00	7.234	0.000	1100	32.481	0.200
Fat (Infiltrated)	2.500	9.00	7.958	0.200	35	15.915	0.100
Heart	4.000	50.00	7.958	0.100	1200	159.155	0.050
Muscle	4.000	50.00	7.234	0.100	7000	353.678	0.100

Tissue	σ	$\Delta\varepsilon_3$	τ_3	α_3	$\Delta\varepsilon_4$	τ_4	α_4
Blood	0.250	1.00E5	159.155	0.200	1.00E7	1.592	0.000
Dry Skin	0.000	0.00E0	159.155	0.200	0.00E7	15.915	0.200
Fat (Infiltrated)	0.035	3.30E4	159.155	0.050	1.00E7	15.915	0.010
Heart	0.050	4.50E5	72.343	0.220	2.50E7	4.547	0.000
Muscle	0.200	1.20E6	318.310	0.100	2.50E7	2.274	0.000

NOTES: The units of τ_1, τ_2, τ_3 and τ_4 are picoseconds (pS), nanoseconds (nS), microseconds (μS) and milliseconds (mS), respectively.

Infiltrated fat refers to fatty tissue that contains tissues of a different type (blood vessels, dermis, muscle, etc.), and as such represents a more physiologically realistic model than does pure (uninfiltrated) fat.

Figure 2-1 illustrates the frequency dependency of the permittivity of the materials whose parameters are given in Table 2-1 and approximated using equation 2-9.

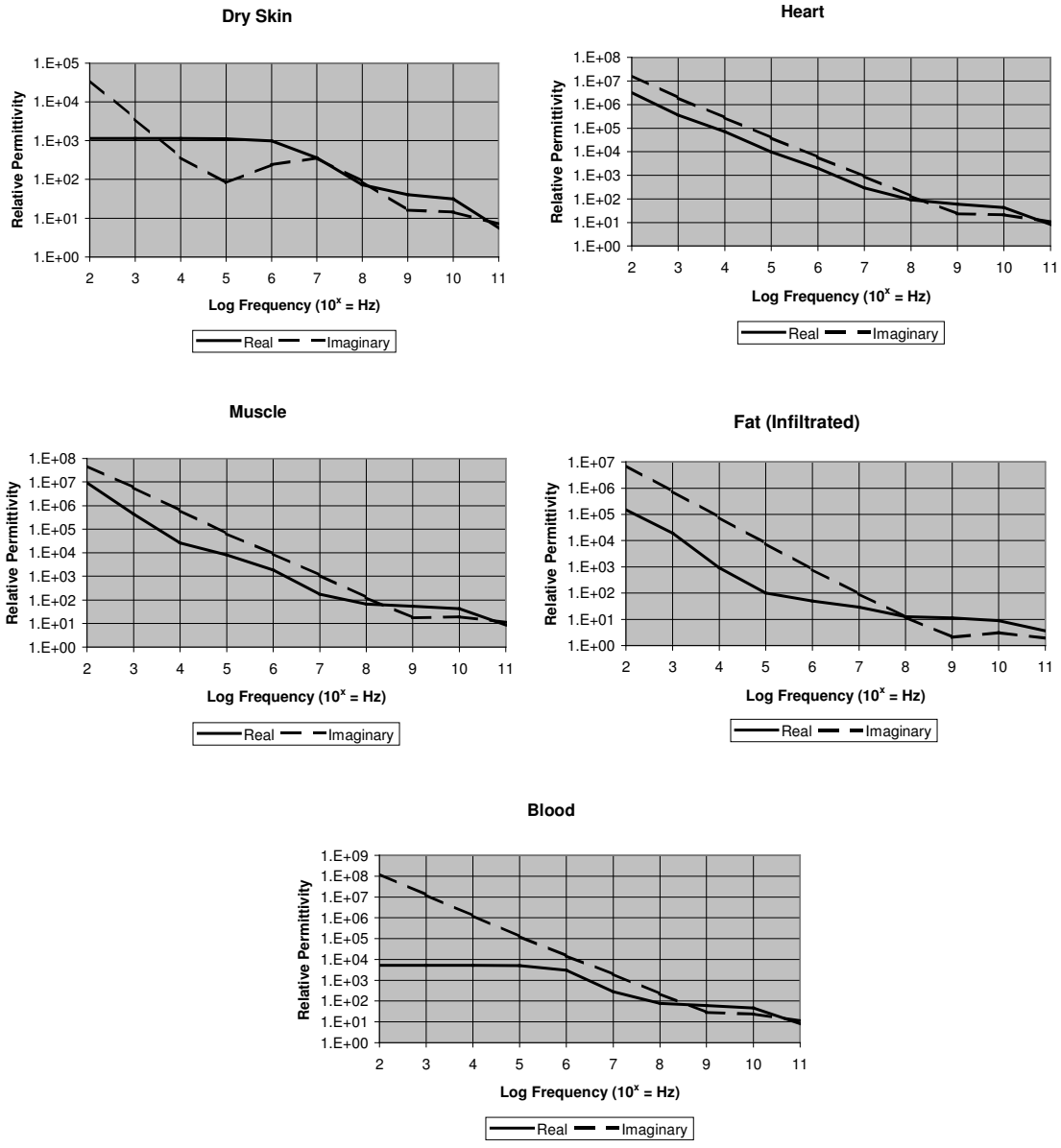

Figure 2-1

Complex Permittivity of Select Biological Materials

Once the complex permittivity for a material has been established (by experimentation, numerical methods, literature search or other means), determination of the remaining parameters needed to characterize and predict propagation behavior through the material can be achieved through fairly simple calculation.

2.3 Conductivity

As shown in [12], the complex relative permittivity ε_r'' is directly dependent on the material conductivity σ, that is

$$\varepsilon_r'' = \frac{\sigma}{\omega \varepsilon_0} \quad , \tag{2-10}$$

where $\omega = 2\pi f$ is the radian frequency (radians per second). Conductivity is easily determined from equation 2-10 using

$$\sigma = \omega \varepsilon_0 \varepsilon_r'' \quad , \tag{2-11}$$

where conductivity σ is in units of S/m. The conductivities of select biological materials, determined using equations 2-9 and 2-11 and the data from Table 2-1, are shown in Figure 2-2.

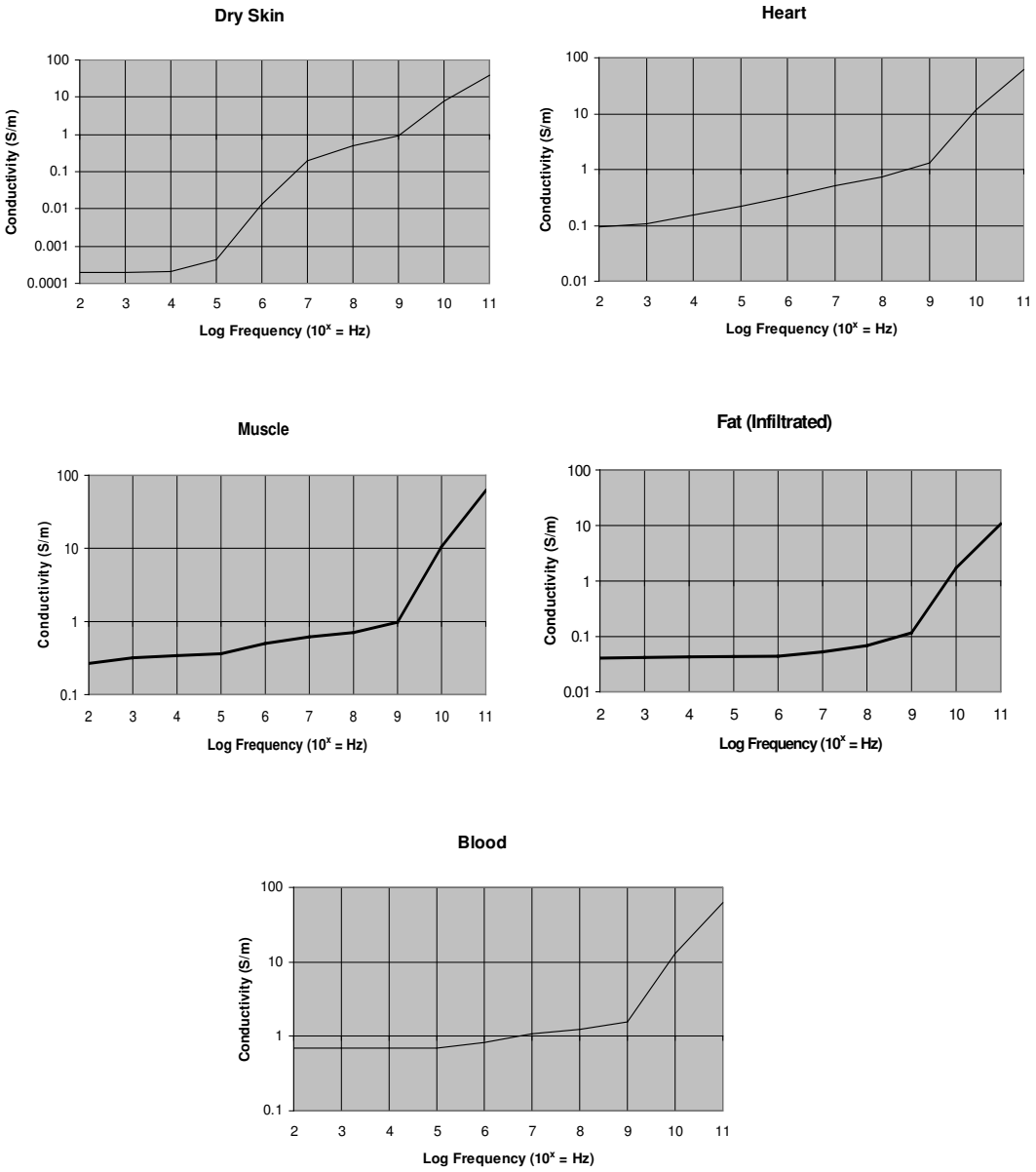

Figure 2-2

Conductivity of Select Biological Materials

2.4 Attenuation

The attenuation constant α (not to be confused with the fitting parameter α in equation 2-9) is most often calculated from theory in units of nepers per meter (n/m), where one neper is approximately equal to 8.686 decibels (dB). For the purposes of this work, where we will be dealing with tissue and organ layers more conveniently measured in millimeters (mm), we will use the conversion

$$\alpha_{dB/mm} \approx 0.008686\ \alpha_{n/m} \quad . \tag{2-12}$$

Attenuation as a function of frequency is determined using [12]

$$\alpha_{n/m} = \left(\frac{\omega}{c}\right)\sqrt{\frac{\mu_r \varepsilon_r'}{2}\left(\sqrt{1+(\varepsilon_r''/\varepsilon_r')^2}-1\right)} \quad , \tag{2-13}$$

or, recalling that biological materials are considered to be non-magnetic (and substituting equation 2-5),

$$\alpha_{n/m} = \left(\frac{\omega}{c}\right)\sqrt{\frac{\varepsilon_r'}{2}\left(\sqrt{1+\tan^2\theta}-1\right)} \quad , \tag{2-14}$$

where c is the speed of light (approximately 2.997925 x 10^8 meters per second). Note that when tan θ is zero (implying a scalar permittivity by equation 2-5), equation 2-14 reduces to zero.

Figure 2-3 shows the bulk attenuation of some biological materials in dB/mm, as a function of frequency.

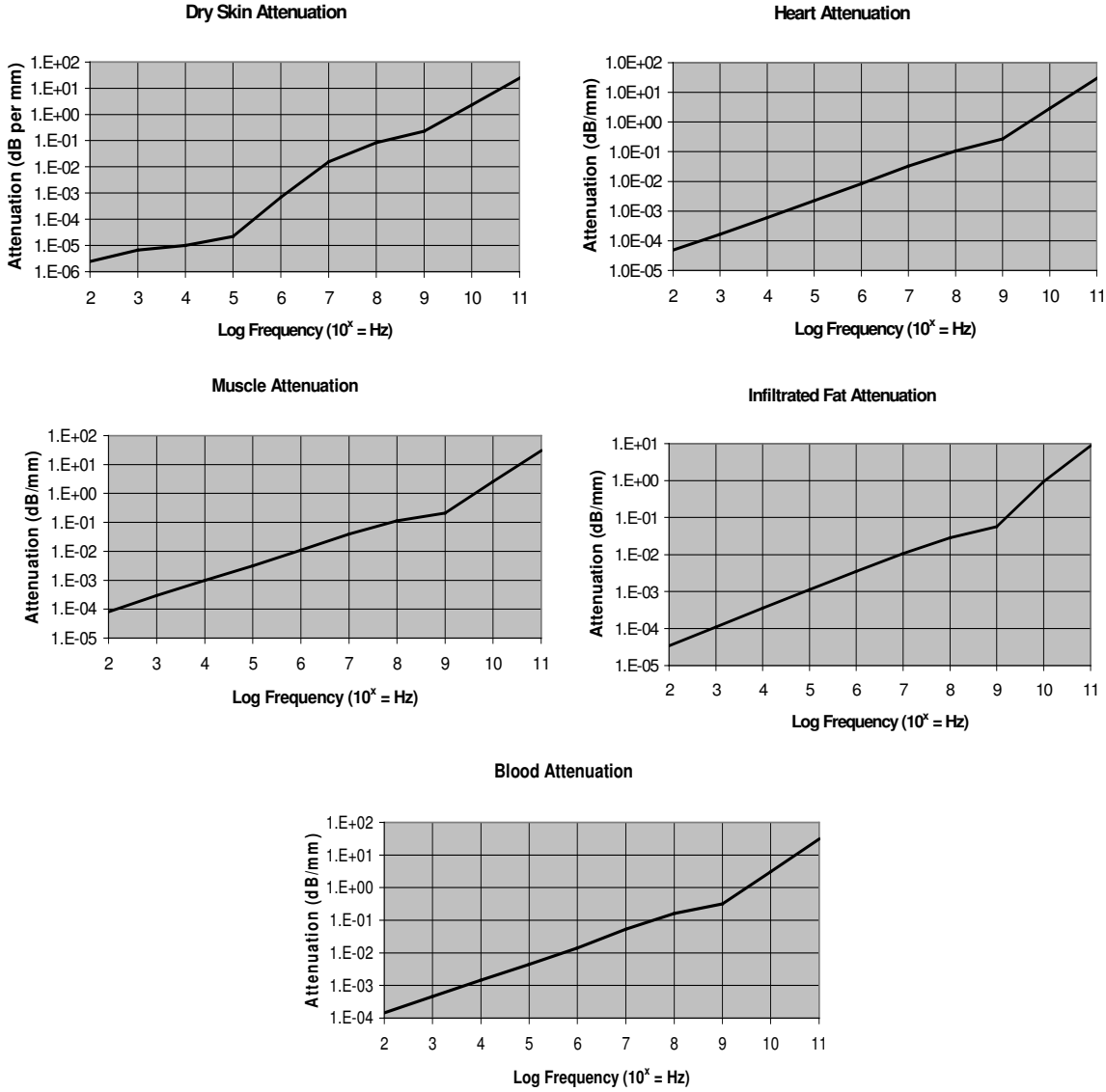

Figure 2-3

Attenuation of Select Biological Materials

2.5 Intrinsic Impedance

The last material property of general interest that we will investigate is that of intrinsic impedance (η). This is understood to be a different quantity than characteristic impedance (Z), since the intrinsic property deals only with the parameters of the material in question and does not necessarily take into account the effects of geometry or boundary conditions.

The intrinsic impedance of free space is found by taking the square root of the ratio of free-space permeability and permittivity; numerically it is given by

$$\eta_0 \approx 376.73 \text{ ohms} \quad . \tag{2-15}$$

For non-magnetic materials with scalar permittivity, the intrinsic impedance is the free-space impedance divided by the square root of the relative permittivity of the material:

$$\eta = \frac{\eta_o}{\sqrt{\varepsilon_r}} \quad . \tag{2-16}$$

To account for the effect of complex permittivity as found in biological materials, we use [12]

$$\eta = \sqrt{\frac{\mu}{\varepsilon'}}\left[\frac{1}{\sqrt{1 - j\tan\theta}}\right] \quad . \tag{2-17}$$

The magnitude of the intrinsic impedance of select biological materials is shown in Figure 2-4.

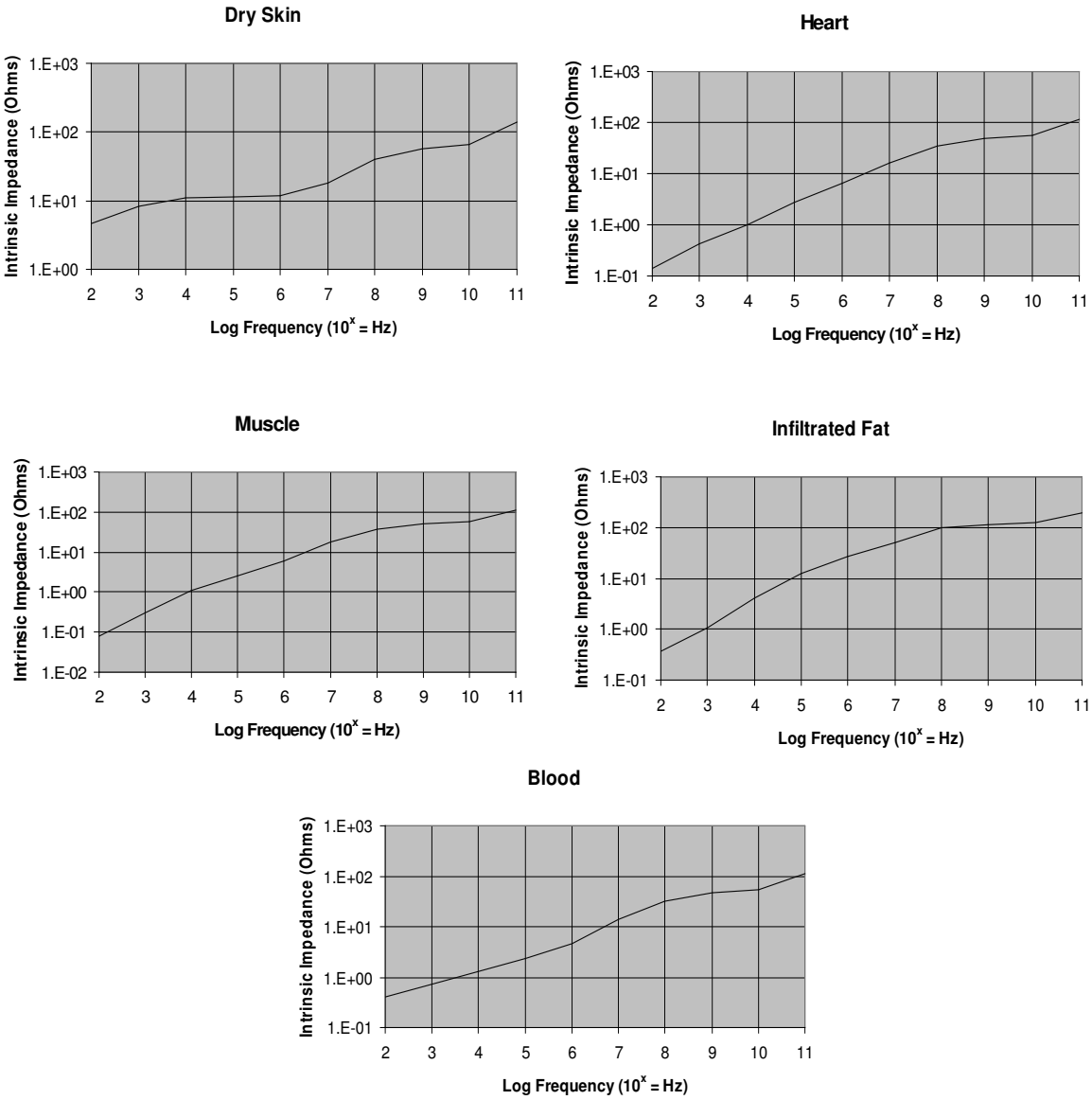

Figure 2-4

Intrinsic Impedance of Select Biological Materials

2.6 Conclusion

With the development of the properties of conductivity, attenuation and impedance (upon measurement or approximation of the complex permittivity), we are now ready to show the application of these properties to studies of specific cutaneous and subcutaneous phenomena, particularly oxygenation and the measurement of internal body temperatures.

Chapter 3

Microwave Sensing of Blood Oxygenation

The effect of oxygen spectral absorption on radio signal transmission in the atmosphere is a well-documented phenomenon [1] – [3]. A series of closely-spaced and often overlapping spectral lines around 60 GHz, referred to as the 60 GHz oxygen complex, has been accurately modeled for the prediction of atmospheric attenuation of RF signals. We will examine several approximation methods in this chapter, and evaluate their applicability to model the signal reflection characteristics of oxygenated blood. After a comparison of the modeling results with experimental test data, we will discuss the potential application of this technique to the detection and diagnosis of skin cancer. We begin with a brief introduction to the molecular resonance mechanism from a quantum mechanical point of view, before moving on to resonance modeling, its application to physiological conditions and potential applications of resonance detection.

3.1 Oxygen Resonances

Resonances are induced by electromagnetic fields, as the energy contained in the field is used to produce transitions in quantum energy states. Oxygen exists in a natural state in molecular form, with two oxygen atoms combining to create an O_2 molecule. This molecule is paramagnetic, with a permanent magnetic moment. Diatomic molecular

spectral absorption is determined by the energy levels dictated by quantum numbers, as shown in Table 3-1, which was created using information from [1].

Table 3-1

Quantum Parameters Affecting Oxygen Resonances

Quantum Number	Description	Behavior in O_2 Molecule
Λ	Electronic Axial Number	Equal to zero
K	Orbital Momentum Number	Only odd values allowed, must remain constant during transition for microwave absorption
S	Molecular Spin Transition Number	± 1
J	Total Angular Momentum (K+S)	J = K-1, K, K+1

All allowable orbital numbers (K = 1, 3, 5 …) and spin transitions ($S = -1 \leftrightarrow 0, 0 \leftrightarrow 1$) result in absorption lines near 60 GHz, with the exception of the transition ($K = 1, J = 0 \rightarrow 1$), which corresponds to approximately 118 GHz [1].

3.2 Resonance Modeling Techniques

The exact characteristics of oxygen resonance are influenced by such parameters as temperature, pressure and water vapor content [1]. These factors very greatly between atmospheric and meteorological measurements and those conditions found in human physiology. These differences in measurement conditions lead to significant discrepancies between atmospheric oxygen absorption lines and blood oxygen resonances.

Two methods of O_2 resonance approximation are examined: the reduced line base model of Liebe [16] and Rosenkrantz' theory of overlapping lines [17]. Each of the methods uses a set of major O_2 spectral line frequencies, with line width, strength and interaction determined by such parameters as oxygen partial pressure (pO_2), water vapor partial pressure (pH_2O) and temperature.

3.2.1 Reduced Line Base Model

Liebe's method is a practical means of approximating oxygen absorption at frequencies below 350 GHz, and is based on evaluation of the imaginary part $N''(f)$ of the complex refractivity. The absorption coefficient α is determined from this quantity using

$$\alpha = (2\omega/c)(10\log e)N''(f) \text{ (dB per mm)} , \tag{3-1}$$

where

$c \approx 2.997925 \times 10^8$ is the free-space speed of light,

$e \approx 2.7182818$ is the natural logarithm base,

f is the frequency is GHz, and

$N''(f)$ is the imaginary portion of the complex refractivity.

The quantity $N''(f)$ is approximated as

$$N''(f) \approx \sum_i S_i F_i(f) + N''_d(f) + N''_w(f) \quad , \tag{3-2}$$

where

i is an index counter of the spectral line used in the calculation,

S_i is the strength of the ith line,

$F_i(f)$ is the shape factor of the ith line as a function of frequency, and

$N''_d(f)$ and $N''_w(f)$ are the dry and wet continuum spectra, respectively.

The line strength S_i is calculated using

$$S_i = a_{1i} p t^3 e^{a_{2i}(1-t)} \quad , \tag{3-3}$$

where

a_{1i} is the line width coefficient for the ith line as given in Table 3-2,

p is the atmospheric pressure in millibars (mbar),

t is the temperature coefficient given by 300/Temp (Kelvin), and

a_{2i} for the ith line is given in Table 3-2,

and the line shape factor $F_i(f)$ is given by

$$F_i(f) = \frac{f}{f_i}\left[\frac{\Delta f - s(f_i - f)}{(f_i - f)^2 + (\Delta f)^2} + \frac{\Delta f - s(f_i + f)}{(f_i + f)^2 + (\Delta f)^2}\right] , \tag{3-4}$$

where

f_i is the frequency of the ith line as given in Table 3-2,

Δf is the width of the line, and

s is a line interference correction factor.

The term "line width" as used above refers to the spectral width (in Hertz) of a specific resonance line. The width is affected by a variety of factors, including excitation quantum level uncertainty, atmospheric pressure broadening, Doppler broadening and Zeeman broadening (due to the earth's magnetic field) [18]. In equation 3-4, the line width factor Δf is found using

$$\Delta f = a_{3i}(pt^{0.8} + 1.1et) \quad , \tag{3-5}$$

where

a_{3i} is the width coefficient of the ith line from Table 3-2, and

e is the water vapor partial pressure in millibars, and

s is found using

$$s = a_{4i}\, pt^{a_{5i}} \quad , \tag{3-6}$$

where coefficients a_{4i} and a_{5i} are given in Table 3-2.

The dry air continuum function $N''_d(f)$ is given by

$$N''_d(f) = fpt^2 \left\{ \frac{6.14\times10^{-5}}{d\left[1+(f/d)^2\right]\left[1+(f/60)^2\right]} + 1.4\times10^{-11}(1-1.2\times10^{-5} f^{1.5})\, pt^{1.5} \right\} \quad , \tag{3-7}$$

where d is a line width parameter determined by

$$d = 5.6\times10^{-4}(p+1.1e)t^{0.8} \quad . \tag{3-8}$$

Finally, the wet air continuum function $N''_w(f)$ is given by

$$N''_w(f) = 1.8\times10^{-8}(p + 30.3et^{6.2})fet^3 + 2.3\times10^{-10}\,pe^{1.1}t^2 f^{1.5} \quad . \tag{3-9}$$

Values for the coefficients specified in equations 3-3 through 3-6 are given in Table 3-2. An implementation of the Reduced Line Base Method, written in MATLAB, is shown in Appendix B.

Table 3-2

Liebe Parameters for Oxygen Resonance Lines

(Adapted from [19])

i	f_i	a_{1i}	a_{2i}	a_{3i}	a_{4i}	a_{5i}
1	51.5034	6.08	7.74	8.90	5.60	1.8
2	52.0214	14.14	6.84	9.20	5.50	1.8
3	52.5424	31.02	6.00	9.40	5.70	1.8
4	53.0669	64.10	5.22	9.70	5.30	1.9
5	53.5957	124.70	4.48	10.00	5.40	1.8
6	54.1300	228.00	3.81	10.20	4.80	2.0
7	54.6712	391.80	3.19	10.50	4.80	1.9
8	55.2214	631.60	2.62	10.79	4.17	2.1
9	55.7838	953.50	2.12	11.10	3.75	2.1
10	56.2648	548.90	0.01	16.46	7.74	0.9
11	56.3634	1344.00	1.66	11.44	2.97	2.3
12	56.9682	1763.00	1.26	11.81	2.12	2.5
13	57.6125	2141.00	0.91	12.21	0.94	3.7
14	58.3269	2386.00	0.62	12.66	-0.55	-3.1
15	58.4466	1457.00	0.08	14.49	5.97	0.8
16	59.1642	2404.00	0.39	13.19	-2.44	0.1
17	59.5910	2112.00	0.21	13.60	3.44	0.5
18	60.3061	2124.00	0.21	13.82	-4.13	0.7
19	60.4348	2461.00	0.39	12.97	1.32	-1.0
20	61.1506	2504.00	0.62	12.48	-0.36	5.8
21	61.8002	2298.00	0.91	12.07	-1.59	2.9
22	62.4112	1933.00	1.26	11.71	-2.66	2.3
23	62.4863	1517.00	0.08	14.68	-4.77	0.9
24	62.9980	1503.00	1.66	11.39	-3.34	2.2
25	63.5685	1087.00	2.11	11.08	-4.17	2.0
26	64.1278	733.50	2.62	10.78	-4.48	2.0
27	64.6789	463.50	3.19	10.50	-5.10	1.8
28	65.2241	274.80	3.81	10.20	-5.10	1.9
29	65.7648	153.00	4.48	10.00	-5.70	1.8
30	66.3021	80.09	5.22	9.70	-5.50	1.8
31	66.8368	39.46	6.00	9.40	-5.90	1.7
32	67.3696	18.32	6.84	9.20	-5.60	1.8
33	67.9009	8.01	7.74	8.90	-5.80	1.7
34	118.7503	945.00	0.00	15.92	-0.13	-0.8

NOTES: All a_1 coefficients are to be multiplied by 10^{-7}.
All a_3 and a_4 coefficients are to be multiplied by 10^{-4}.

3.2.2 Theory of Overlapping Lines

Rozenkrantz's formulation is an attempt to reduce the complexity of the resonance calculations by simplifying the spectral line width – pressure relationship as expressed in other approximation methods. Using this method, the absorption function $\kappa_{O2}(f)$ (which is analogous to the attenuation coefficient α in section 3.2.1) is found using

$$\kappa_{O_2}(f) = 1.61\times10^{-8} f^2 \left(\frac{P}{1013}\right)\left(\frac{300}{T}\right)F' \quad \text{(dB per mm)} \ , \tag{3-10}$$

where

f is the frequency in GHz,

P is the pressure in millibars, and

T is the absolute temperature in Kelvin.

The function F' accounts for line strength and spectrum shape. A summation is used over odd values of the quantum number N (only the first 39 terms are considered significant), and F' is determined by

$$F' = \frac{\gamma_b}{f^2 + \gamma_b^2} + \sum_{N=1,3,5...}^{39} \Phi_N \left[g_{N+}(f) + g_{N+}(-f) + g_{N-}(f) + g_{N-}(-f) \right] \ , \tag{3-11}$$

where $g_{N\pm}(f)$ is given by

$$g_{N\pm}(f) = \frac{\gamma_N (d_{N\pm})^2 + P(f - f_{N\pm})Y_{N\pm}}{(f - f_{N\pm})^2 + \gamma^2{}_N} \quad , \tag{3-12}$$

and Φ_N is

$$\Phi_N = 4.6\times10^{-3}\left(\frac{300}{T}\right)(2N+1)\times\exp\left[-6.89\times10^{-3}N(N+1)\left(\frac{300}{T}\right)\right] \quad . \tag{3-13}$$

The quantities γ_b and γ_N in equations 3-11 and 3-12 are nonresonant and resonant line width parameters, respectively, and are expressed as

$$\gamma_b = 0.49\left(\frac{P}{1013}\right)\left(\frac{300}{T}\right)^{0.89} \tag{3-14}$$

and

$$\gamma_N = 1.18\left(\frac{P}{1013}\right)\left(\frac{300}{T}\right)^{0.85} \quad . \tag{3-15}$$

In equation 3-12, the quantities d_{N+} and d_{N-} are the amplitudes of the f_{N+} and f_{N-} lines, respectively, and are given by

$$d_{N+} = \left[\frac{N(2N+3)}{(N+1)(2N+1)} \right]^{0.5} \tag{3-16}$$

and

$$d_{N-} = \left[\frac{(N+1)(2N-1)}{N(2N+1)} \right]^{0.5} \quad . \tag{3-17}$$

Values for the resonant frequencies f_{N+} and f_{N-} and interference parameters Y_{N+} and Y_{N-} are given in Table 3-3. An implementation of the Overlapping Line Method, written in MATLAB, is shown in Appendix C.

Table 3-3

Rozenkrantz Parameters for Oxygen Resonance Lines

(Adapted from [20])

	Frequencies (GHz)		Interference ($mbar^{-1}$)	
N	f_{N+}	f_{N-}	Y_{N+}	Y_{N-}
1	56.2648	118.7503	4.51	-0.214
3	58.4466	62.4863	4.94	-3.78
5	59.5910	60.3061	3.52	-3.92
7	60.4348	59.1642	1.86	-2.68
9	61.1506	58.3239	0.33	-1.13
11	61.8002	57.6125	-1.03	0.344
13	62.4112	56.9682	-2.23	1.65
15	62.9980	56.3634	-3.32	2.84
17	63.5685	55.7838	-4.32	3.91
19	64.1278	55.2214	-5.26	4.93
21	64.6789	54.6711	-6.13	5.84
23	65.2241	54.1300	-6.99	6.76
25	65.7647	53.5957	-7.74	7.55
27	66.3020	53.0668	-8.61	8.47
29	66.8367	52.5422	-9.11	9.01
31	67.3694	52.0212	-10.3	10.3
33	67.9007	51.5030	-9.87	9.86
35	68.4308	50.9873	-13.2	13.3
37	68.9601	50.4736	-7.07	7.01
39	69.4887	49.9618	-25.8	26.4

NOTE: All Y_{N+} and Y_{N-} coefficients are to be multiplied by 10^{-4}.

3.2.3 Modeling Evaluation

In order to verify the proper implementation of equations (3-1) and (3-10), we used the source code shown in appendices B and C, respectively, to evaluate a well-documented atmospheric condition: that of 60 GHz attenuation at sea level and ambient temperature, using conditions of Standard Temperature and Pressure (STP) [21]. The results for each approximation method are shown in Figure 3-1. The frequency, magnitude and shape of the atmospheric oxygen attenuation curve are in excellent agreement between methods, and with those data previously published [1] - [3].

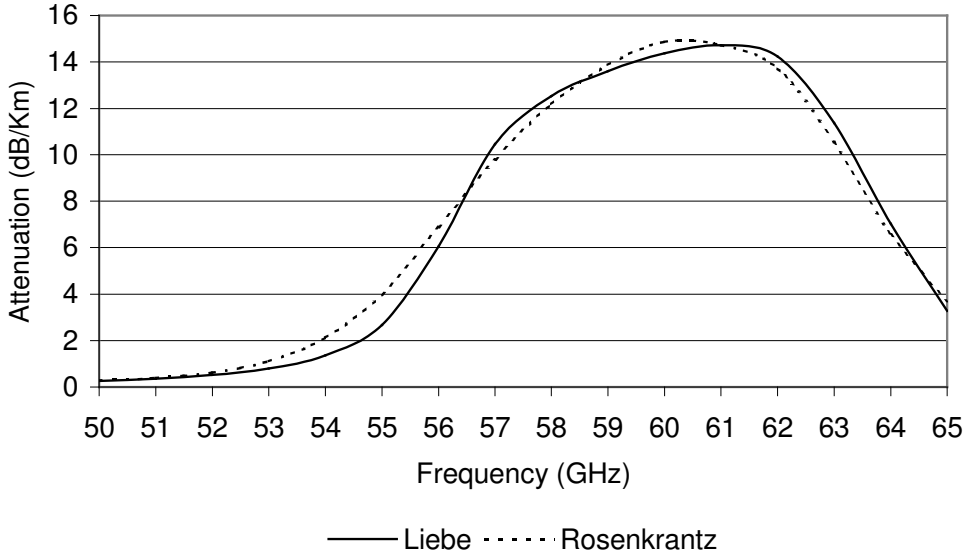

Figure 3-1

Sea Level Atmospheric Oxygen Modeling Evaluation

3.3 Blood Oxygen Characteristics

In section 3.2 we presented two means of oxygen resonance approximation using methods of atmospheric attenuation modeling, and verified each of those methods by comparing their results with those already published for sea level atmospheric attenuation. Before we can apply these equations to estimate the effect of resonances due to tissue oxygenation, we must first investigate the quantitative differences between atmospheric conditions and those that exist within the human physiology. Only then may we be able to apply the proper parameters that will yield a usable model of the responses expected from human tissue.

In order to adequately describe the oxygenation of blood and quantify the differences between blood and atmospheric oxygenation, however, we must first present some basic material on the relevant aspects of the physiology of the respiratory system. These aspects include changes in oxygen and water vapor content during inspiration (breathing in), conditions within the lung, and the blood-gas barrier within the alveoli and terminal capillaries.

Within a mixture of gasses, such as the atmosphere we breathe, there exists a set of partial pressures: each corresponding to one of the gasses in the mixture. Dalton's Law states that the partial pressure of a specific gas within a mixture is the same as if that gas alone occupied the total volume, in the absence of the other gasses. Stated another way, we can consider the partial pressure of a single gas in a mixture to be the

contribution the pressure of that gas makes to the total pressure of the mixture. For example, the pressure of the earth's atmosphere at sea level is approximately 760 millimeters of mercury (760 mmHg). Oxygen comprises about 21% of the atmosphere by volume, so the partial pressure of oxygen (pO_2) at sea level is the product of concentration and total pressure, or about $0.21*760 \approx 160$ mmHg [22].

Upon inspiration, atmospheric air is warmed and moistened until the water vapor partial pressure (pH_2O) is 47 mmHg [22]. The increase in water vapor content reduces the dry gas pressure from 760 to 713 mmHg. This in turn reduces the pO_2 from 160 mmHg to $0.21*713 \approx 150$ mmHg. Once the inspired air has reached the alveoli for transfer to the blood, the pO_2 has fallen to approximately 100 mmHg [23]. This is due to the continual transfer of oxygen from the inspired air to the non-oxygenated blood. (The term "non-oxygenated" is used here in a relative sense, because venous blood typically has a pO_2 of about 40 mmHg; lower than that of arterial blood but non-zero, nonetheless). Blood is very efficiently re-oxygenated as it passes through the alveolar capillaries, so that the pO_2 of arterial blood is also 100 mmHg [24]. Figure 3-2 shows a schematic representation of oxygen partial pressure as it progresses from the atmosphere, passes through the lungs and blood, and ultimately reaches body tissues [23].

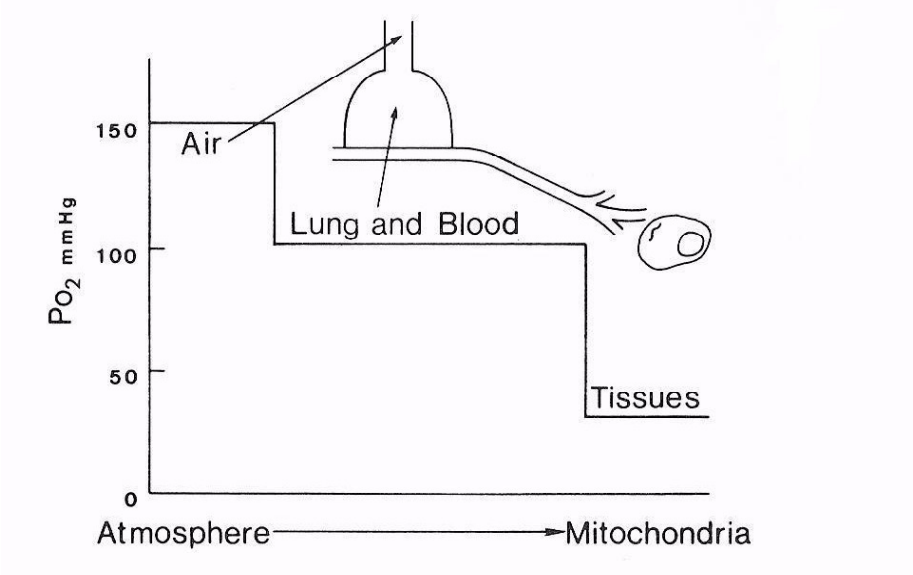

Figure 3-2

Oxygen Partial Pressures from Air to Tissues

(Used with Permission)

By convention, blood gasses are measured at any temperature and pressure, then converted to the values they would have at body temperature (37 C) and pressure (sea level minus water vapor pressure), known as Body Temperature Pressure Saturated (BTPS). This condition includes the parameters and values shown in Table 3-4 [25].

Table 3-4

BTPS Conditions for Arterial Blood

Temperature	37°C
pO_2	100 mmHg*
pH_2O	47 mmHg

*Standard sea level atmosphere assumed.

3.4 Approximation Results

The data and equation sets for the Liebe and Rozenkrantz approximation methods were evaluated over the frequency range of 50 to 65 GHz, and the results are shown in Figure 3-3. Partial pressure data as given in Table 3-4 for arterial blood were used. A comparison of Figure 3-1 for sea level atmospheric oxygen and Figure 3-3 for arterial blood oxygen shows an attenuation of the resonance peaks under blood conditions and the emergence of separate resonance lines due to lower blood pO_2 [26]. The results for the expected oxygen resonances in arterial blood demonstrate excellent agreement between the approximations, with major spectral responses between 58.3 and 62.4 GHz and a peak at approximately 60.4 GHz.

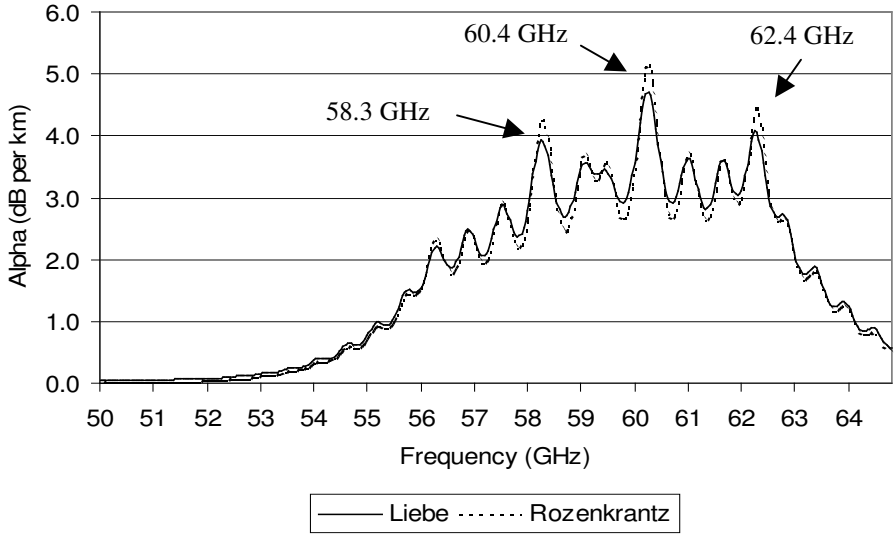

Figure 3-3

Comparison of Oxygen Attenuation (Absorption) Results Under Arterial Blood Conditions

3.5 Blood Resonance Measurements

We obtained samples of fresh bovine blood from a local slaughterhouse for testing. The sample was prepared using a standard sodium heparin preservative [27] and kept refrigerated when not under test. Data were collected using an Anritsu 37397C Vector Network Analyzer (VNA) calibrated for a signal reflection measurement (S_{11}) using a short-open-load (SOL) method with the VNA test port 1 serving as the reference plane. A 60 GHz 1" square aperture horn antenna and waveguide-coaxial adapter performed the signal input and output functions. The sample was placed into a small zip-lock poly bag, which was positioned on a steel shorting plate. The antenna aperture was then placed directly on the poly bag, as shown in Figure 3-4.

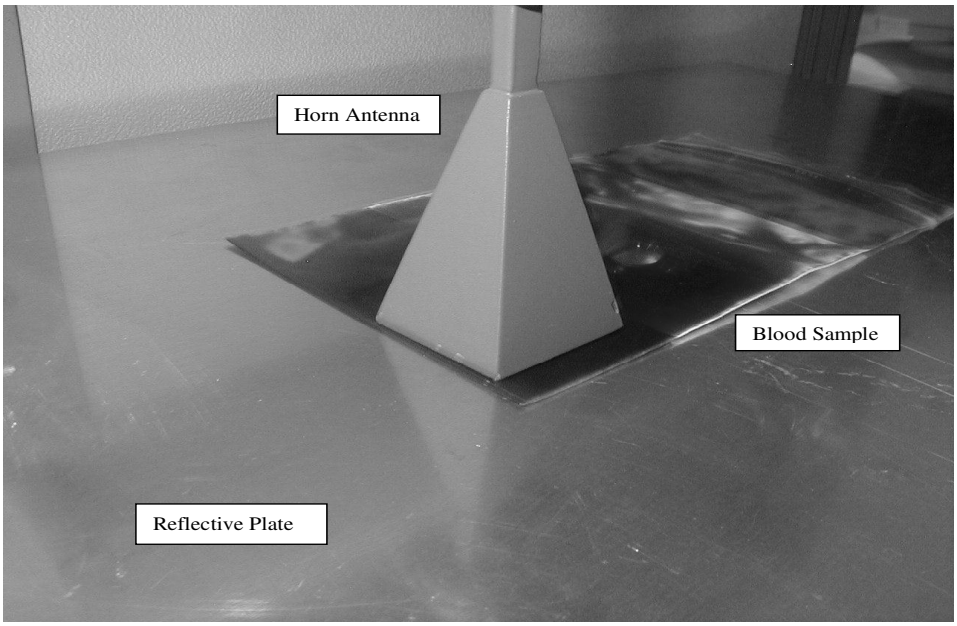

Figure 3-4

Oxygen Resonance Sample Test Setup

Blood exhibits a number of resonances in the range of 50 – 65 GHz, as shown in the return loss data plot of Figure 3-5. Major resonance lines occur at approximately 51, 54, 55, 58 and 65 GHz. Although the causes of these lines are not yet known, it is suspected that the spectra of non-oxygen blood components are contributing factors. For example, Rogacheva *et al.* have speculated that the 55 and 65 GHz resonances are due to the hydrogen-bond networks of subsurface water in proteins [4].

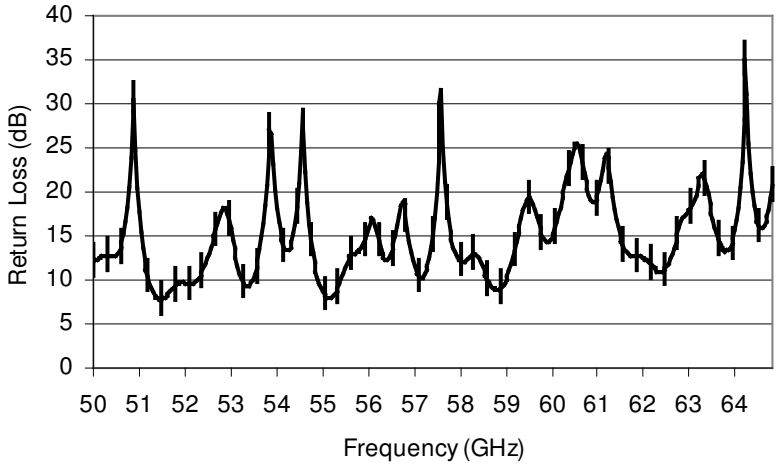

Figure 3-5

Bovine Blood Resonances from 50 – 65 GHz (Sample Age 90 Minutes)

(Error Bars Indicate Sample Variability, N = 6)

We are able to offer supporting evidence to the argument that some of the response peaks observed in this frequency range are due to the presence of water. Figure 3-6 shows a plot similar to that shown in Figure 3-5, except that the bovine blood sample has been replaced in turn with distilled water and ethanol. A comparison of these two plots reveals that distilled water also displays response peaks at approximately 51, 54 and 55 GHz, while the ethanol trace is relatively flat at these frequencies. Subsequent data, which appear later in this section, suggest that the frequencies of the peaks may be dependent on the test setup structure, particularly the thickness of the blood sample.

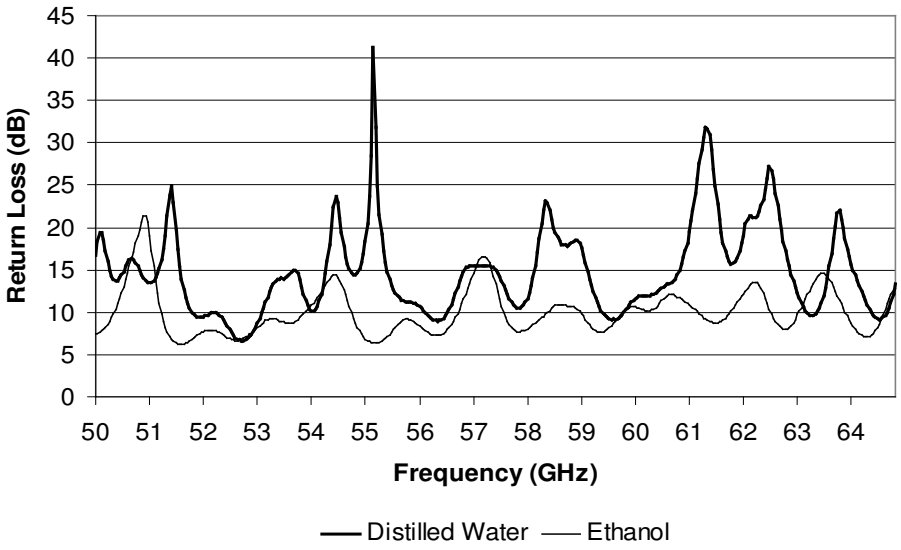

Figure 3-6

Distilled Water and Ethanol Resonances from 50 – 65 GHz

With the exception of the frequency region near 60 GHz, the blood resonance characteristics are largely unchanged as testing is repeated after 24 and 48 hours, as shown in Figure 3-7. A slight upward frequency shift in the 24 and 48 hour data is compensated in Figure 3-7 by shifting the curves downward approximately 112 MHz and 262 MHz, respectively. Although a cursory examination in the area near 60 GHz might suggest a change in response with time, we performed an integration of the differences over time in 1 GHz increments to ensure there was a delta. This integration was performed using the algorithm

$$\sum_{i=1}^{N} \frac{|\Gamma_i|}{N} \quad , \tag{3-18}$$

where *N* is the number of datapoints taken per GHz of frequency sweep. Since data were collected in intervals of 0.0375 GHz, *N* is approximately equal to 27. Comparisons were made between the reflection magnitude data from fresh blood to that at 24 hours age (Figure 3-8a) and to that at 48 hours age (Figure 3-8b). In both cases, the response difference reached a maximum value around 60 to 62 GHz, giving objective evidence of maximal change in that range of frequencies.

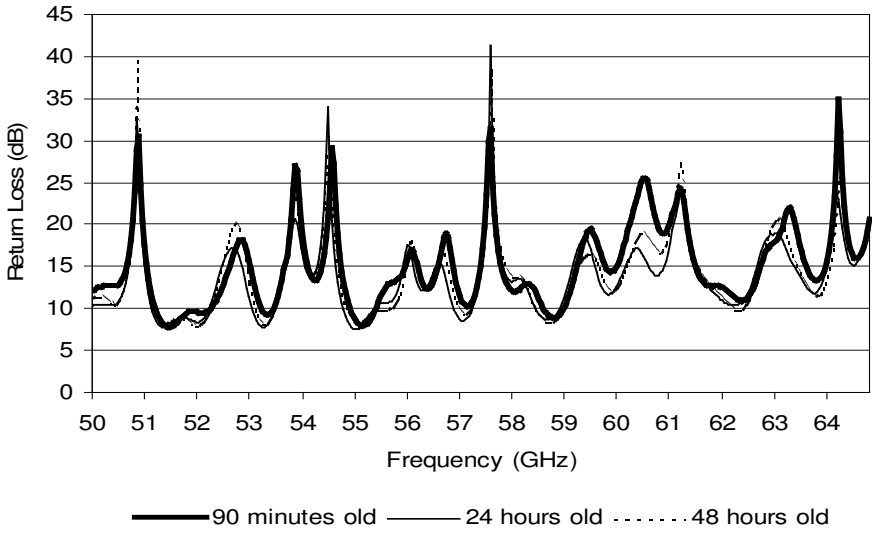

Figure 3-7

Bovine Blood Resonances from 50 – 65 GHz

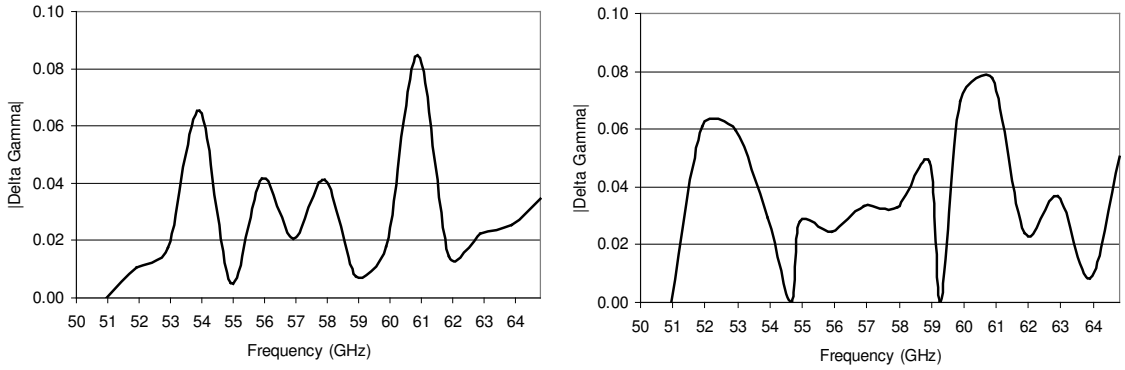

a.) b.)

Figure 3-8

Blood Response Changes with Age (Integration Analysis)

(a = Fresh to 24 hours, b = Fresh to 48 hours)

A moving average analysis of the data also shows a maximum change in response over time. The analysis was performed over 50 datapoints using each set of differences in the magnitude gamma data, as used for Figure 3-8. The results of this analysis are shown in Figure 3-9a (for the first 24 hours after extraction) and Figure 3-9b (for the first 48 hours after extraction). As with the integration analysis, the results of the moving average analysis show that the maximum change in reflected magnitude over time occurs in the frequency range of 60 to 62 GHz.

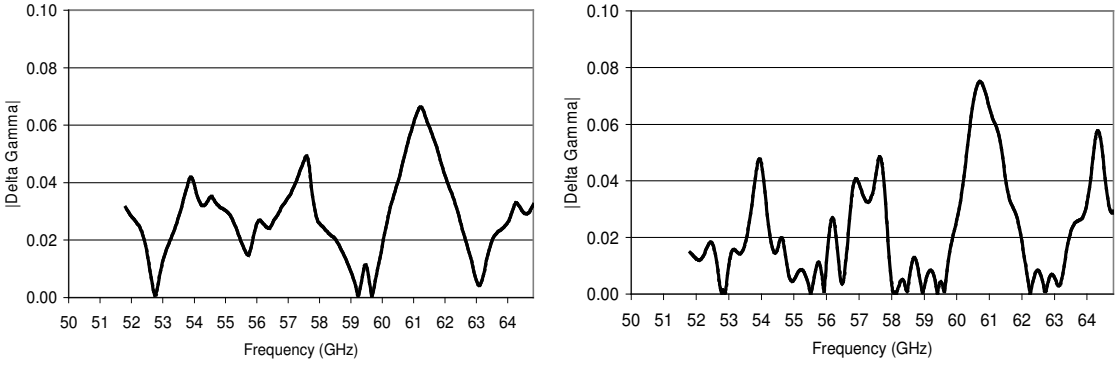

a.) b.)

Figure 3-9

Blood Response Changes with Age (Moving Average Analysis)

(a = Fresh to 24 hours, b = Fresh to 48 hours)

When we superimpose the Liebe approximation on the resonance data, as in Figure 3-10, the contribution of O_2 resonance to the blood response becomes evident.

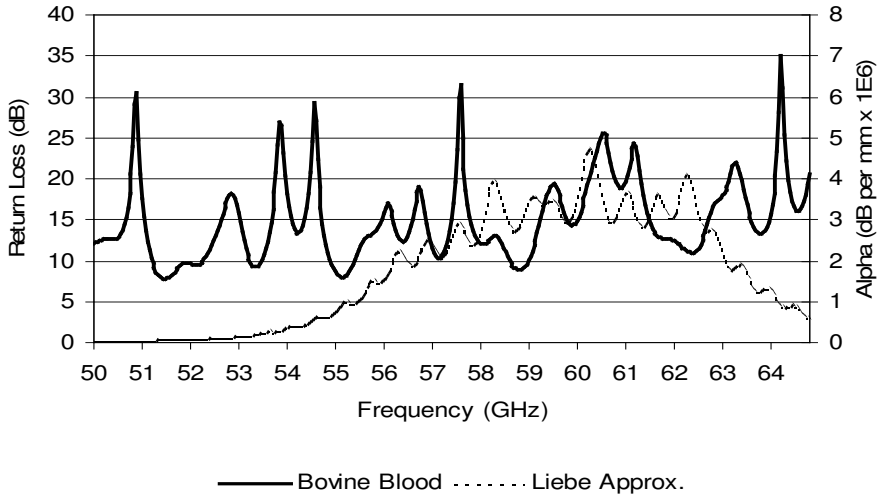

Figure 3-10

Bovine Blood Resonances with O_2 Attenuation Superimposed

(Measured Data Quantized in Scale on Left, Oxygen Attenuation on Right)

It is apparent by examination of Figure 3-10 that the resonances at 51, 54, 55 and 64.5 GHz are not caused by the presence of oxygen in the blood. In Figure 3-11, the frequency range of 60 – 61.5 GHz is examined more closely.

The presence of a different system of units between the left and right y-axes in Figures 3-10 through 3-11 and Figure 3-13 is not intended to imply a numerical equivalency between the two quantities. They are placed in juxtaposition simply to demonstrate that the return loss and attenuation peaks in blood occur at substantially the same frequencies.

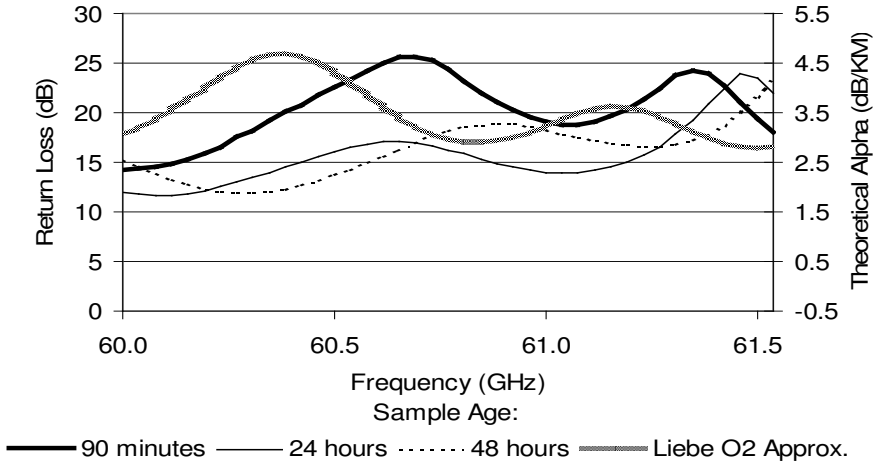

Figure 3-11

Bovine Blood Resonances with O_2 Attenuation Superimposed (60 – 61.5 GHz)

(Measured Data Quantized in Scale on Left, Oxygen Attenuation on Right)

The theoretical resonance curve and the curve at 90 minutes sample age show good agreement in terms of relative peak amplitudes, width and spacing. The frequency

difference of about 300 MHz between the approximation and data at 90 minutes is attributed to the shift in measurement reference planes that was incurred with the addition of the waveguide-coaxial adapter and horn antenna. As expected due to the effect of aging, degradation of the oxygen content is evident after 24 hours. This effect is predicted by the metabolic rate of drawn blood at 4°C. Since the pO_2 of *in vitro* blood decreases by 0.01% volume every 10 minutes [28], the oxygen partial pressure is reduced by approximately 1.5 volumes percent over a twenty-four hour period. Correspondence between the oxygen response and resonance approximation curves is almost non-existent at 48 hours sample age.

We performed several series of tests in order to verify that the results suggested by the preliminary data are due to oxygen resonance and variability rather than a secondary effect. In one set of tests, we subjected samples of materials lacking the oxygen molecule to the identical test procedure and conditions under which we measured the blood samples. These materials included:

Distilled water (H_2O)

Isopropyl alcohol ($CH_3CHOHCH_3$)

Ethanol (C_2H_6O)

The test results for these materials are shown in Figure 3-12. The results demonstrate the differences between the expected O_2 resonances and the spectral response of each of the

non-oxygenated materials, in that the double peak response of the oxygen approximation is missing from each of the materials under test.

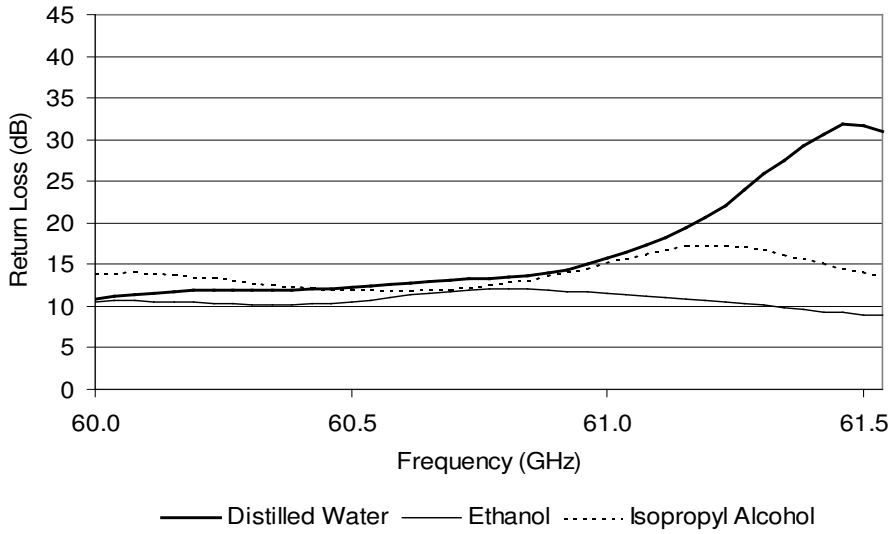

Figure 3-12

Non-Oxygenated Material Responses with O_2 Attenuation Superimposed

We also subjected samples of Complete Rapid QC© arterial blood gas calibration solution [29] to the identical test procedure and conditions under which we measured the bovine blood samples. Complete is a tri-level buffered bicarbonate solution with specific values of pO_2 for each level, as specified in the manufacturer's data sheets and summarized in Table 3-5.

Table 3-5

Complete Rapid QC© Solution Level Descriptions

Complete Level	pO_2 (mm Hg)	Blood Condition Similarity
1	139 – 145	Atmospheric pO_2 (Hyperoxygenated)
2	91 – 102	Arterial pO_2 (Normal O_2)
3	22 – 25	Depleted pO_2 (Hypooxygenated)

The test results for these materials are shown in Figure 3-13. The figures show a similar pattern between the Complete data and the bovine blood data shown in Figures 3-7 and 3-11, in that the two resonance peaks between 60 and 61.5 GHz decrease in amplitude with decreasing levels of oxygen. This supports our contention that oxygen is the cause of the shifting peaks in the bovine blood data in Figure 3-7.

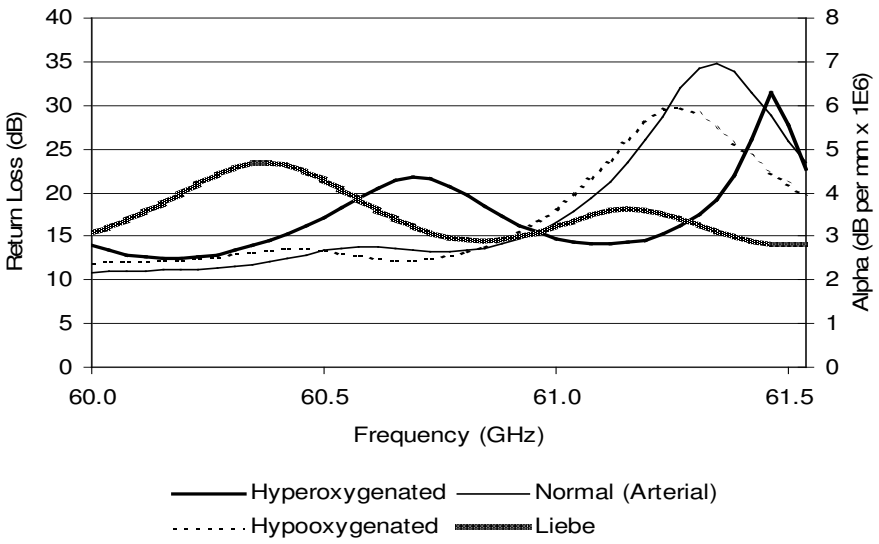

Figure 3-13

Complete Calibration Sample Responses with O_2 Attenuation Superimposed

(Measured Data Quantized in Scale on Left, Oxygen Attenuation on Right)

A question was raised during the course of the research as to the effect of the surrounding atmosphere on the validity of the measurements. Observing Figure 3-4 carefully, we note that the antenna aperture does not come into direct contact with the metal shorting plate. Consequently, the test structure as implemented does not represent a shielded enclosure, and atmospheric effects may be introduced to the data by means of the antenna sidelobes. To preclude this possibility, we designed a shielded fixture similar to an offset short, which would minimize antenna sidelobe leakage by placing the antenna aperture completely and directly in contact with the shorting plate. An aperture-sized recess is located concentrically with the aperture shelf, which allows several milliliters of

test liquid to the subjected to 60 GHz irradiation. The fixture and its implementation are shown in Figure 3-14.

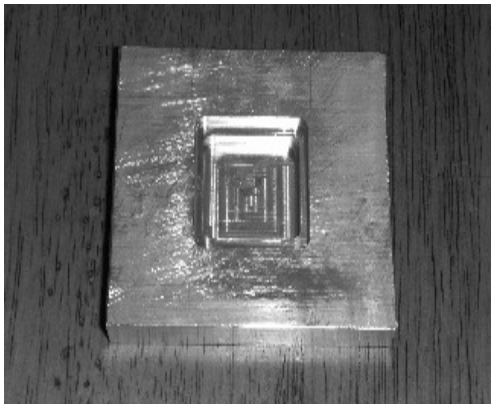

a.) Fixture as designed

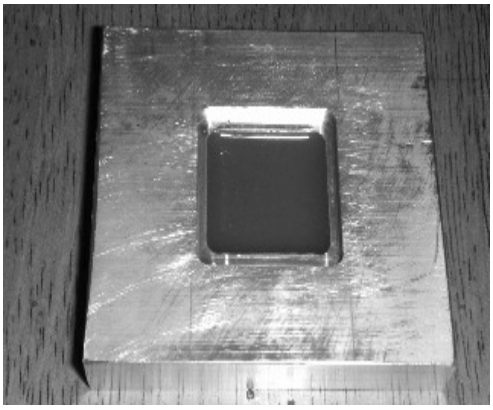

b.) Fixture with liquid

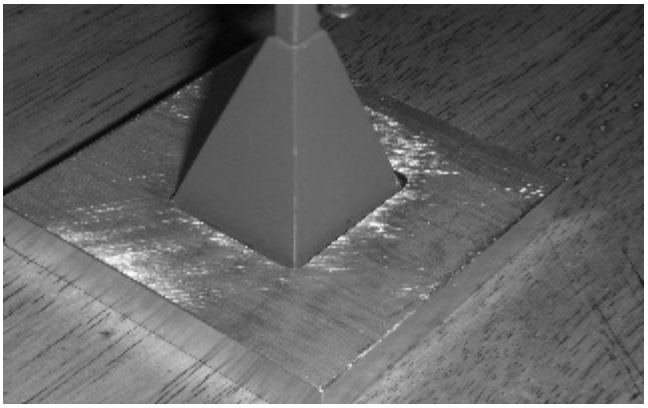

c.) Fixture with antenna

Figure 3-14

Antenna Shorting Plate/Test Fixture

Data obtained when using this fixture are shown in Figure 3-15, for Complete Level 1 and Level 2 solutions (hyper- and normal oxygen levels, respectively). The test was also repeated for non-oxygenated materials as in Figure 3-12; these results are shown in

Figure 3-16. The presence of the characteristic “double peak”, with decreasing magnitude corresponding to decreasing oxygen level, is evidence of the validity of the prior test data (Figures 3-5 to 3-7).

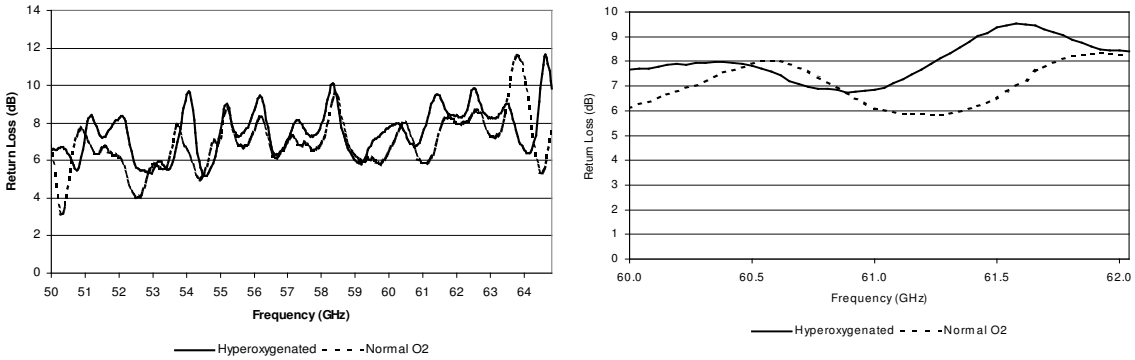

a.) 50 – 65 GHz b.) 60 – 62 GHz

Figure 3-15

Blood Oxygen Calibration Sample Data Using Test Fixture

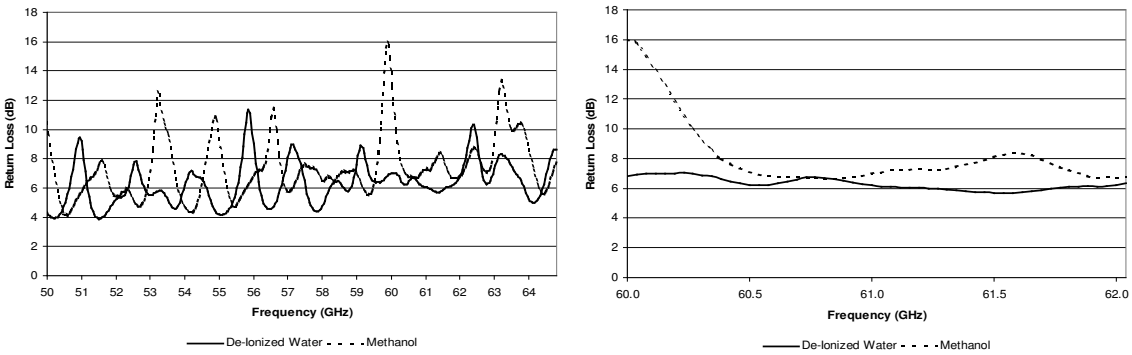

a.) 50 – 65 GHz b.) 60 – 62 GHz

Figure 3-16

Non-Oxygenated Materials Data Using Test Fixture

Figure 3-15 offers further evidence of a shift in peak frequency due to thickness of the test material. In Figure 3-13, where the data were collected using the plate setup of Figure 3-4, the calibrator solution with normal oxygenation levels displayed response peaks at frequencies of 60.6 and 61.4 GHz. Figure 3-15b shows the result of the same solution tested in the fixture shown in Figure 3-14. Under this condition, the frequency of the upper peak has shifted to 61.9 GHz. The most significant difference between these two conditions is the thickness of the calibrator sample under test. When tested with the shorting plate as a backing, the sample thickness was approximately 2.5 mm. The test chamber in the fixture has a depth of 4.5 mm. Since the difference in sample thicknesses corresponds to approximately 0.4 wavelengths in free space (and an even greater percentage of wavelength in the sample material), this magnitude of change in the signal path length could certainly contribute to such a shift in response frequencies.

3.6 Blood Permittivity Measurements

The successful measurements that had been conducted to this point involved the construct of a relatively thin planar layer of blood backed by some form of metallic short circuit. This configuration was chosen for several reasons: to accommodate the horn antenna aperture of approximately one square inch while simulating as closely as possible the small amount of blood expect *in vivo*, and to provide a highly reflective background against which any resonances would be readily observed. However, we could not discount the possibility that this construct may introduce its own set of resonances due to

the physical dimensions of the fixturing in combination with the propagation characteristics of the material under test.

In order to verify that the resonances we observed were due to the properties of blood oxygenation and not the test methods, we measured the permittivity of bovine blood in bulk, 24 hours after extraction, using open-ended coaxial probes. No reflective ground plane was used, and the thickness of the blood layer was not constrained as it was during resonance testing. For this series of tests, we used the slim form probe option of the Agilent 85070 Dielectric Measurement System as controlled by the Agilent E8361C vector network analyzer. The probe consisted of a 6-inch length of RG405 semirigid coaxial cable, with one end terminated with a 1.85mm coaxial connector and simple flush cut which served as the calibration reference plane on the opposite end. The calibration procedure was provided by the Dielectric Measurement software, and consisted of a reflection (S_{11}) calibration using short (copper strip), open (air) and load (deionized water) as impedance references. The permittivity test probe implementation is shown in Figure 3-17.

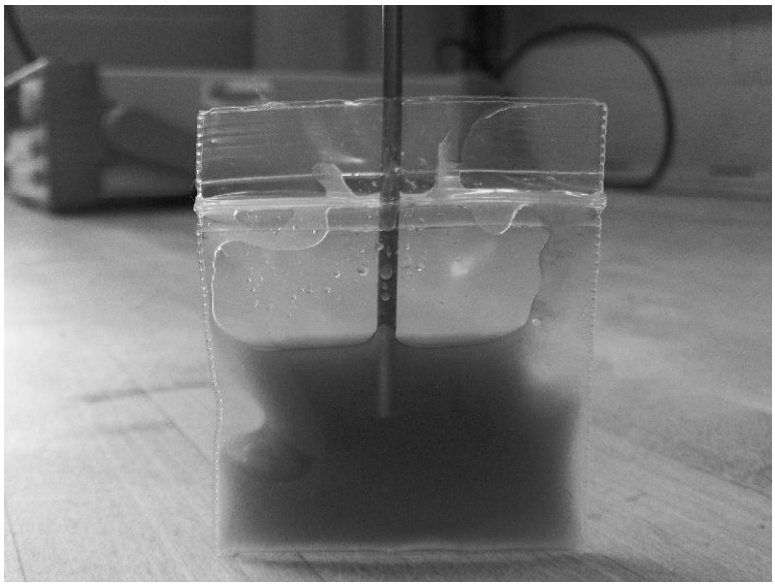

Figure 3-17

Permittivity Test Probe in Sample

The blood permittivity test results are shown graphically in Figure 3-18. The curve shows a plot of the blood loss tangent as a function of frequency, as defined by equation 2.5, with the Gabriel database approximation [10], [12] shown as a dashed line. This ratio maintains a relatively constant value of approximately 1.2 to 1.4 with frequency, with the exception of two prominent non-linearities, centered at approximately 61.2 and 61.8 GHz. These non-linearities are not predicted by the results of the fourth-order Cole-Cole expression (eq. 2-9). Again, it would appear that the primary resonant frequencies have changed from earlier results; however, as previously mentioned, the thickness of the test sample was not constrained in the test setup of Figure 3-17, while it had been during testing per Figures 3-4 and 3-14.

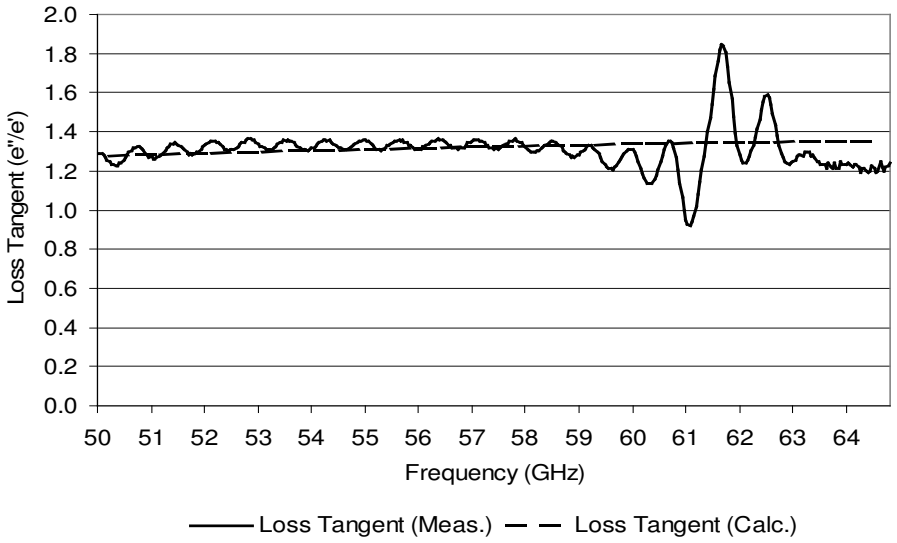

Figure 3-18

Blood Loss Tangent

(Blood Age 24 Hours)

3.7 Software Simulation Results

Finally, we simulated the reflection response of a planar blood layer using Agilent High Frequency Structure Simulator (HFSS) software, version 11. Blood was simulated using the permittivity data from Figure 3-18 in tabular form (as shown in Appendix D) as data file inputs. Due to the frequency-dependent nature of the electrical characteristics of blood, a discrete sweep was used, requiring a complete electromagnetic solution to be computed at each test frequency. Figure 3-19 shows the simulation setup; the antenna dimensions were based on physical measurements of the antenna shown in Figure 3-4.

The bottom of the test sample, which is not visible in the figure, is modeled as a perfectly reflecting plane. This simulation was based on the test setup of Figure 3-4.

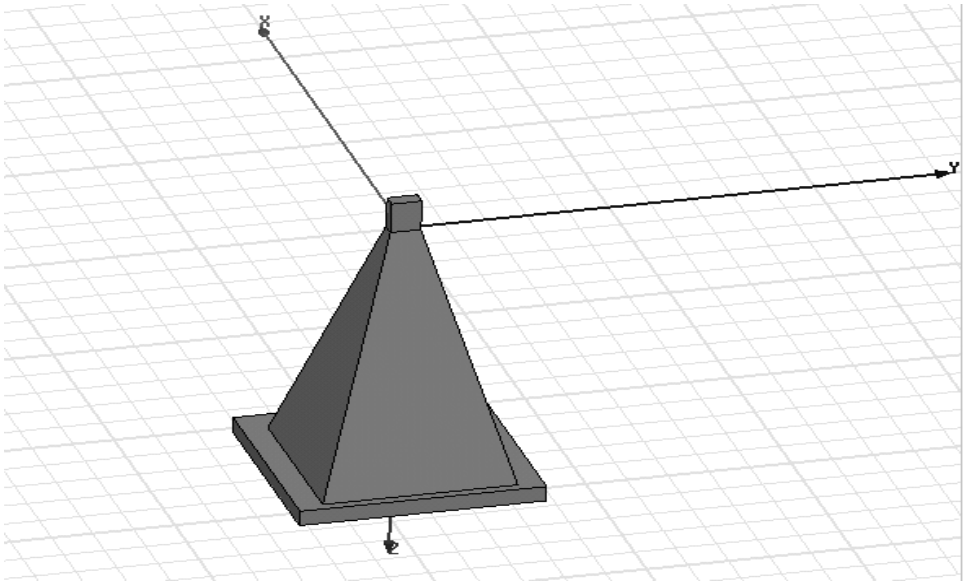

Figure 3-19

Test Simulation in HFSS

The results of the simulation are shown in Figures 3-20 and 3-21. Figure 3-20 shows the simulated blood response from 50 to 65 GHz. Since the blood sample used to take the permittivity data in Figure 3-18 was 24 hours old, a comparison was made with the measured blood data taken 24 hours after extraction. The figure shows good correspondence between the two curves.

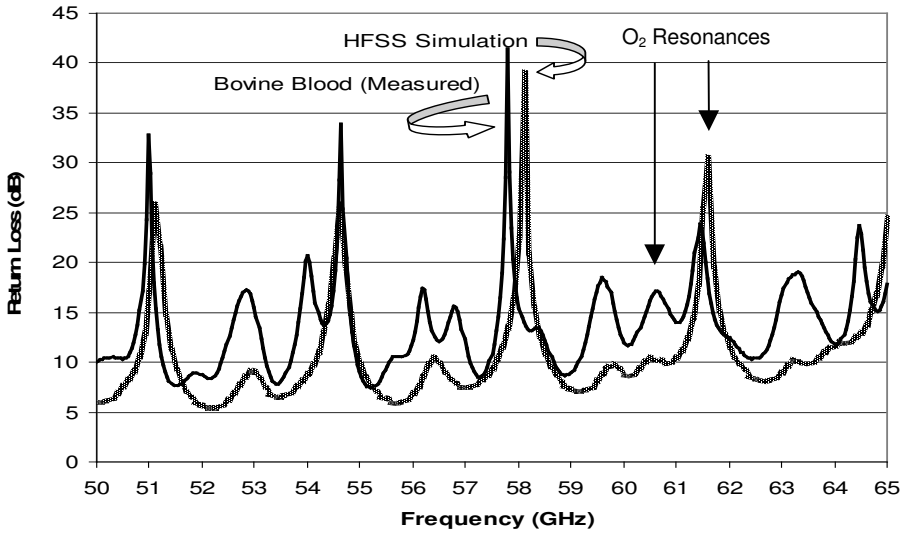

Figure 3-20

HFSS Simulation of Bovine Blood Response

The major peaks in the simulated and measured responses in Figure 3-20 coincide quite well, both in terms of amplitude and frequency. The minor peaks are less pronounced in the simulation than in the measured data. This could be due to the finite nature of the permittivity data that defined the blood material (401 points from 50 to 65 GHz), to the fact that the simulation frequency set did not coincide with that of the permittivity data (due to computational restraints), or to a combination of the two factors.

In Figure 3-21, the HFSS simulation is plotted with the bovine blood and Complete calibrator data corresponding to normal arterial blood oxygenation. The close

correspondence between the three curves in this figure justifies our conclusion that blood oxygenation may be directly detected by means of the 60 GHz oxygen resonance complex.

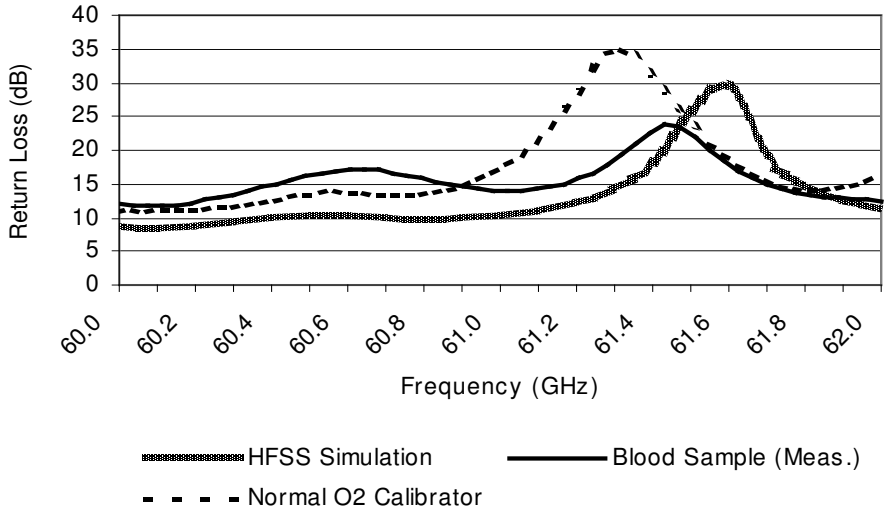

Figure 3-21

Resonance Comparison: Blood Simulation, Measurement and Calibrator Data

3.8 Skin Attenuation

None of the preceding analyses or results are of benefit to an *in vivo* test situation if the attenuation inherent in the skin precludes detection of the data. In order to ensure that this is not the case, we revisit equation 1-14 and use the data in Table 1-1. In Figure 3-22, the expected attenuation of skin at 60 GHz is shown to be about 18 dB per mm. In section 3.9 we will show that useful *in vivo* data can be obtained at millimeter penetration depths. Allowing for the fact that we are using reflection measurements, this means that

the 60 GHz signal travels through approximately 2 mm of skin, giving an expected attenuation of 36 dB. This value is within the dynamic range of commercially available test equipment, as shown in Appendix E [30].

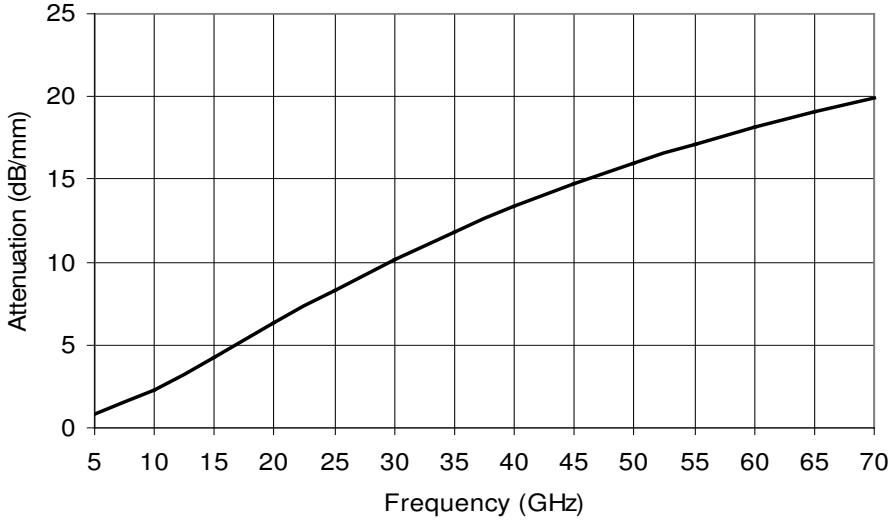

Figure 3-22

Predicted Signal Attenuation in Skin as a Function of Frequency

3.9 Application to Skin Cancer Detection

The ability to detect blood oxygen could be of advantage in the detection of skin cancer. Angiogenic activity in the vicinity of tumors is well documented [31], [32]. Angiogenesis refers to the ability of living tissue to initiate the construction of new blood vessels to provide oxygen and nutrients for growth. Research has shown that angiogenesis is required for cancerous tumors to grow and metastasize. One potential use of blood oxygen detection in this application is to employ elevated oxyhemoglobin levels

as a marker for increased blood flow, thereby detecting possible angiogenic activity near a suspected tumor. Our intent is to increase the incidence of early screening and detection, by developing a technology that will indicate malignant areas painlessly, non-invasively and in real time, thereby reducing financial and anxiety-based impediments to cancer screening.

3.9.1 Motivation

The presence of skin cancer is a common yet deadly phenomenon, especially in a climate such as that found in Florida, where the combination of intense sunlight and year-round outdoor activities greatly increases the chances of overexposure to ultraviolet rays. The following facts are provided by the Skin Cancer Foundation [33]:

More than 1.3 million skin cancers are diagnosed yearly in the United States.
One in 5 Americans and one in 3 Caucasians will develop skin cancer in the course of a lifetime.
Survival rate for those with early detection is about 99%. The survival rate falls to between 15 and 65% with later detection depending on how far the disease has spread.
In the past 20 years there has been more than a 100% increase in the cases of pediatric melanoma.
After thyroid cancer, melanoma is the most commonly diagnosed cancer in women 20-29.

3.9.2 Dimensional Requirements

The goal of this effort is to detect lesions before they have metastasized. According to the Tumor, Node, Metastasis (TNM) system of classification [34], melanoma rarely metastasizes when its thickness is less than 1 mm. This corresponds to tumor classification levels T1a and T1b, which represent the newest, or least developed tumors. In practical terms, this sets an upper limit of 1 mm for the depth penetration requirement of this technology. This is on the order of typical epidermal thickness in areas where skin cancer commonly develops: 0.5 mm over most of the body [35] to 0.05 mm on the eyelids and postauricular areas [36].

The spatial resolution necessary for this technology to be effective is determined by the criteria set forth in the Asymmetry, Border, Color, Diameter and Evolution (ABCDE) guidelines of self-examination [37]. These guidelines state that any skin growth greater than 6 mm in diameter could be abnormal. Consequently, this requires the spatial resolution of this technology to be capable of detecting abnormalities no larger than 6 mm in diameter.

The technology described in this chapter is capable of meeting both these dimensional requirements. As shown in the previous section, the attenuation of skin in the 60 GHz oxygen complex is about 18 dB per mm. Given an early-stage tumor depth of 1 mm, this will result in a reflected signal attenuation of about 36 dB, which does not

preclude detection using existing equipment. Secondly, the free-space wavelength of a 60 GHz signal is approximately 5 mm, which is less than the size of the tumors being detected. Further, this wavelength will decrease in body tissues due to a non-unity value of relative permittivity, increasing the signal resolution capability further into the useful region below 6 mm.

3.9.3 Background/Literature Review

Previous techniques for non-invasive skin examination include low-frequency impedance measurements and visual light spectroscopy.

3.9.4 Impedance Spectroscopy

Beetner *et al.* looked at detecting basal cell carcinoma using impedance spectroscopy. They successfully classified skin samples as being normal, benign lesions or malignant basal cell carcinoma by focusing on skin lesions ranging from 2 to 15 mm diameter [38]. The study showed that, while impedance differences were found between malignant lesions, benign lesions and normal skin, the differences were not sufficiently conclusive to establish clear identification of the lesion based solely on impedance measurements. This was attributed to the relatively small size of the lesions compared with that of the contact probe.

In a similar study that compared basal cell carcinoma to benign pigmented cellular nevi, Åberg *et al.* also concluded that statistical differences exist between the impedance of common skin lesions and that of normal skin, although further development is needed for the technique to be useful as a diagnosis tool [39].

3.9.5 Visible Light Spectroscopy

Other research efforts have used lightwave technology to determine the malignancy of skin lesions. Mehrübeoğlu *et al.* used light at wavelengths of 500 to 800 nm to differentiate benign skin lesions from those exhibiting malignancy [40]. However, due to the limited depth of penetration inherent in using frequencies of this wavelength, this technique is limited to those tumors which lie directly on the visible surface of the skin.

Cui *et al.* proposed the use of wavelengths longer than those of visible light, in order to increase the penetration depth of the signal. This proposal is reasonable, considering the reflection and transmission characteristics of viable skin. As wavelength increases (implying decreasing frequency), the reflection coefficients decrease. This decrease results in greater effective depths of penetration for longer wavelength (lower-frequency) signals, while maintaining attenuation at workable levels [41].

Cui's proposal led to this area of research, using microwave signals, which until now has been relatively unexplored. We have shown that microwave signals provide the spatial resolution needed to detect Level T1 tumors, while maintaining signal attenuation

sufficiently low as to obtain data at skin depths associated with cutaneous and sub-cutaneous malignancies.

3.10 Future Work

We would like to repeat the resonance measurements already performed using an antenna with a smaller aperture than that being used. The present antenna has an aperture size of approximately 645 mm^2 (one square inch); this is satisfactory for the bulk measurements being made to date, but larger than many Level T1 tumors and can lead to *in vivo* test results that are ambiguous or false. The use of a smaller radiating and receiving aperture will allow us to verify the spatial resolution of the 60 GHz signal, and will confirm the utility of this technique for identifying malignancies that are the size of skin cancers. With the success of a small aperture antenna this research should, with appropriate regulatory approval, progress to animal studies (for example, characterization of papilloma virus in laboratory mice).

3.11 Conclusion

We have demonstrated a method for the measurement of oxygen in blood by detecting changes in the 60 GHz resonance spectra. This may be useful in performing non-invasive measurement of tissue oxygenation or hemoglobin concentration in the vicinity of tumors. This technique can be employed for evaluation of a variety of other

skin conditions in which oxygenation levels play a part, including but not limited to the study of burn and wound healing, contact-induced pressure points and the detection and treatment of psoriasis [42].

Chapter 4

Radiometric Sensing of Internal Organ Temperature

Microwave radiometry is based on the principle of blackbody radiation: the phenomenon of all objects whose absolute temperature exceeds zero to emit electromagnetic energy. Emission occurs over an extremely wide frequency range, encompassing wavelengths in the radio, infrared, optical, ultraviolet and x-ray spectra. The detection and quantification of this radiated energy in the microwave frequency range, and its subsequent conversion to temperature, is referred to as microwave radiometry. Receiving these emissions in the RF/microwave spectrum involves working with signals possessing extremely low power levels and time-varying characteristics similar to those of noise. In fact, we will show that the RF power emitted by an object at a non-zero absolute temperature is identical to the thermal noise power of a resistor [43]:

$$P = kTB \quad , \tag{4-1}$$

where

P is the thermal noise power in watts,

$k \approx 1.381 \times 10^{-23}$ joule/K is Boltzmann's constant,

T is the temperature in Kelvin, and

B is the frequency bandwidth in Hertz.

Signal emission as a function of temperature has implications for non-contact temperature measurement. The primary motivation in this work is that of internal organ temperature measurement during extended missions in space.

4.1 History and Background

The study of radiometry began with Planck's theory of blackbody radiation, first introduced in the late 19th and early 20th centuries. Non-biological applications of microwave radiometry included radioastronomy and remote sensing. Suggestion of the use of microwave radiometry to the fields of biology and medicine first appeared in the 1970's. In 1974, Bigu del Blanco *et al*. proposed using radiometry to detect changes of state in living systems [44]. Carr also reports that radiometry was used in breast cancer research in the 1970's. Early theoretical work in tissue radiothermometric measurement was performed in the 1980's by Plancot, *et al*. (1984), Miyakowa, *et al*. (1981), and Bardati, *et al.* (1983) [45]. It was reported in 1989 that radiometry in biological applications was being studied with limited but promising results [46].

Research in the field moved quickly in the 1990's with the development of low-noise transistors capable of operating to 10 GHz. This eliminated the costly and complex need for low-temperature noise sources, which used liquid nitrogen or liquid helium for cooling [47]. By 1995, it was reported that microwave radiometry was being used to

perform rheumatological activities in joints, breast cancer detection and abdominal temperature pattern measurements [48].

4.2 Radiometry Review

The ideal signal source for the study of radiometry is the physically unrealizable concept of a blackbody. A radiator of this type is one that is perfectly opaque (no transmission) and absorbs all incident radiation (no reflection), at all frequencies. Since a blackbody is a perfect absorber, it must also be a perfect radiator at all frequencies, in order to maintain a constant temperature.

Planck's radiation law describes the spectral brightness of a blackbody in terms of frequency and temperature [49]:

$$B = \frac{2hf^3}{c^2}\left[\frac{1}{e^{hf/kT} - 1}\right] \quad , \tag{4-2}$$

where

B is the spectral brightness in Watts/m^2/steradian (sr)/Hz,

$h \approx 6.626 \times 10^{-34}$ joules is Planck's constant,

f is the frequency in Hertz, and

$c \approx 2.997925 \times 10^8$ m/s is the free-space velocity of light.

Figure 4-1 shows a parametric plot of equation 4-2 for frequencies in the low GHz range. The curves in the plot represent absolute temperatures relatively near the normal physiological temperature of the human body (98.6 °F, or 310.15 K) and show variations in blackbody brightness with temperature and frequency.

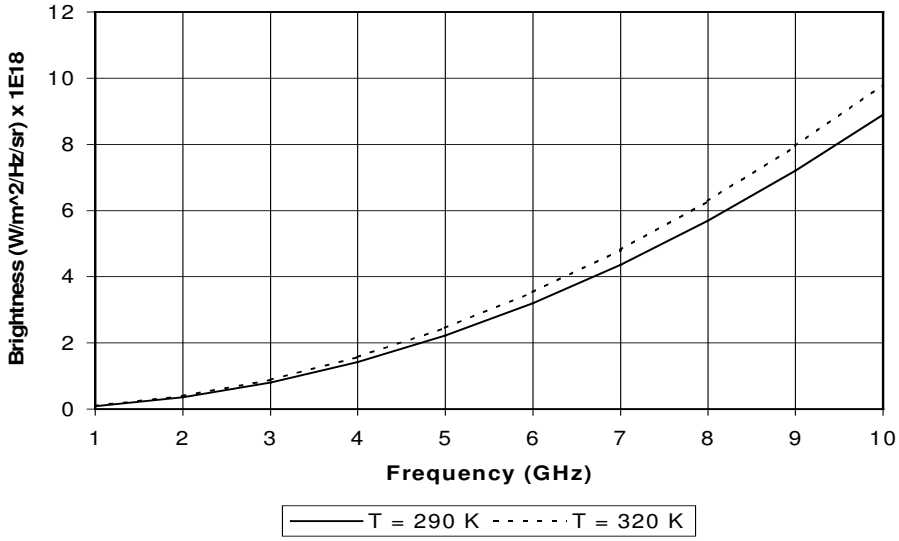

Figure 4-1

Blackbody Spectral Brightness as a Function of Frequency and Temperature

Several approximation methods exist in order to simplify the computation of equation 4-2. One method that is particularly useful for the microwave frequency range is the Rayleigh-Jeans approximation, expressed as [50]

$$B = \frac{2kT}{\lambda^2} \quad , \tag{4-3}$$

where $\lambda = c/f$ is the freespace wavelength of the blackbody emission. Figure 4-2 shows a comparison of Planck's Law and Rayleigh-Jeans approximation results, showing excellent correspondence in the low GHz frequency range.

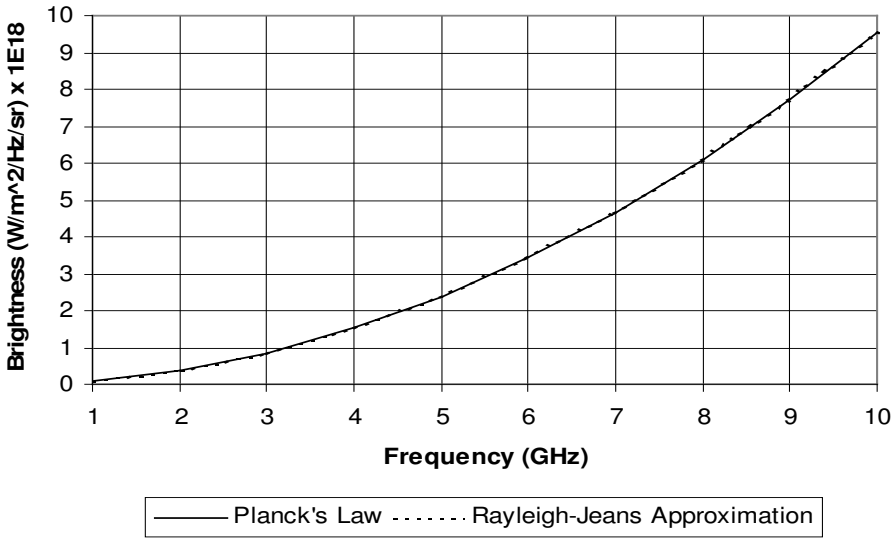

Figure 4-2

Planck's Law and Rayleigh-Jeans Approximation at T = 310 K

The mathematical simplicity of the Rayleigh-Jeans approximation of Planck's Law allows for the derivation of a convenient expression for the power radiated by a blackbody emission. Given that the detection bandwidth Δf is sufficiently narrow to allow the assumption of a constant brightness value with frequency, we can express the received power as [51]

$$P = kT\Delta f \frac{A_r}{\lambda^2}\Omega_p \quad , \tag{4-4}$$

where

P is the received power in watts,

A_r is the antenna area, and

Ω_p is the antenna solid pattern angle.

Since the antenna solid pattern is the ratio of the wavelength squared to the antenna area, equation 4-4 reduces to

$$P = kT\Delta f \quad , \tag{4-5}$$

which is identical to equation (4-1).

The requirement of a small Δf results in emitted power levels that are extremely low. Figure 4-3 shows the power-temperature relationship for an assumed measurement bandwidth of 300 MHz. Note that the emitted power is confined to the picowatt level for the entire range of biological temperatures. The detection of signals of this magnitude requires an extremely sensitive, low-noise receiver as the basis of the radiometer.

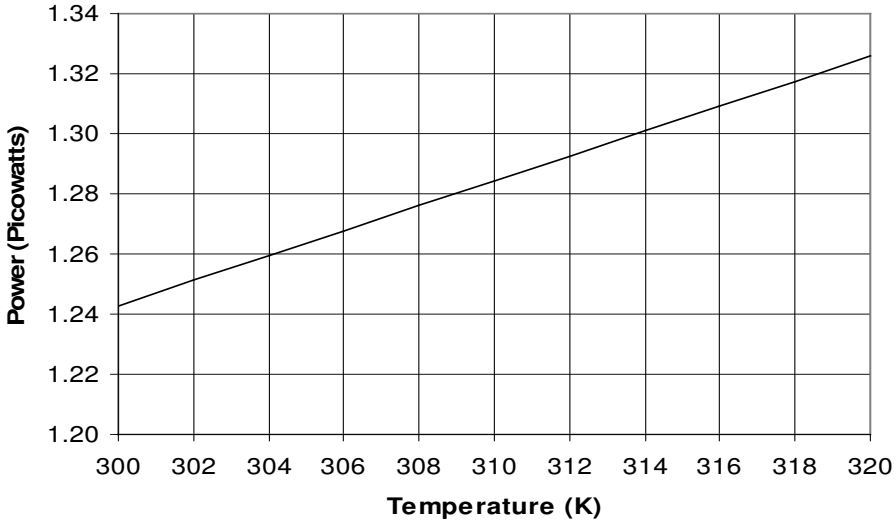

Figure 4-3

Emitted Power vs. Temperature Over a 300 MHz Bandwidth

4.3 Propagation Model

Before we can begin to apply the radiometric principles discussed in section 4.2 to a biological system, we must first expand the principles of blackbody radiation to accommodate multiple materials and temperature gradients as found in human physiology. Considerable theoretical work in the study of thermal emissions from multi-layered structures has already been performed [52], [53], [54]; the derivations presented here follow mainly from [55].

From [56] we know that the effective input noise temperature T_{IN} of a noiseless device at physical input temperature T_1 is related to the noise figure F by

$$T_{IN} = (F - 1)T_1 \quad . \tag{4-6}$$

For the passive materials such as those we will encounter in biological systems, the noise figure F is taken to be equal to the signal attenuation L of the material [57], and equation 4-6 becomes

$$T_{IN} = (L - 1)T_1 \quad , \tag{4-7}$$

where L is related to the signal attenuation in decibels (dB) by

$$L = 10^{-dB/10} \quad . \tag{4-8}$$

Now, assume that the noiseless device (or material layer, for this discussion) is at physical temperature T_H. The temperature emitted from this layer (T_E) is the sum of the material temperature T_H and the input temperature given by equation 4-7, divided by the signal loss of the layer:

$$T_E = \frac{1}{L}\left[T_H + (L-1)T_1\right] \quad , \tag{4-9}$$

which simplifies to

$$T_E = \frac{T_H}{L} + \left(1 - \frac{1}{L}\right)T_1 \quad . \tag{4-10}$$

For a structure consisting of two passive material layers with losses corresponding to L_1 and L_2 (where layer 1 is adjacent to the heat source T_H and T_E is the emitted temperature of layer 2), equation 4-10 can be expanded to

$$T_E = T_H' / L_2 + T_2 (1 - 1/ L_2) \quad , \quad (4\text{-}11)$$

where T_H' is given by

$$T_H' = T_H / L_1 + T_1(1 - 1/ L_1) \quad , \quad (4\text{-}12)$$

and

T_E represents the temperature emitted by the structure

T_H is the elevated temperature of the internal organ (T_0 in Figure 4-3), and

L_1 and L_2 are the losses introduced by layers 1 and 2, respectively.

We are now ready to begin a first approximation analysis of the radiometric characteristics of simple biological structures.

4.4 Biological Model

Figure 4-4 shows an illustration of the radiometry problem [57]. An internal organ at elevated temperature (the heart, in this example) is separated from the radiometer antenna by several layers of biological tissue. Each layer is assumed to have its own temperature (T) and propagation loss (L) characteristics. Further, the layers are

considered homogeneous in that the temperature and loss characteristics are not functions of position within the layer.

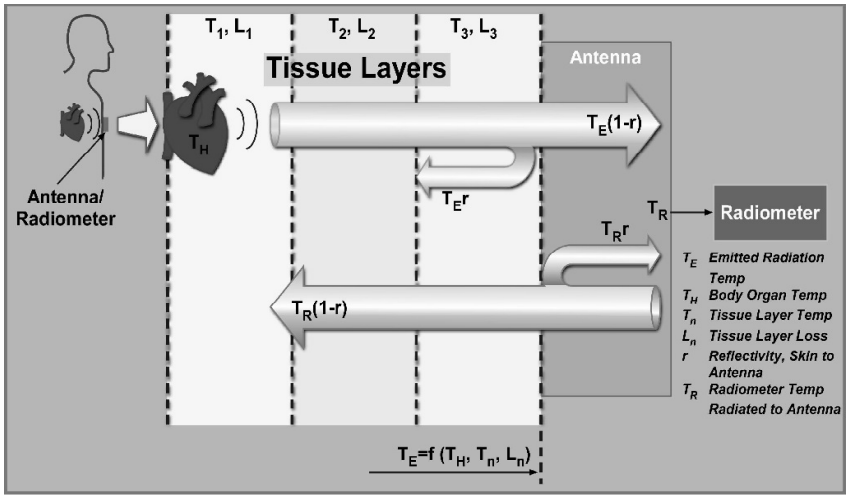

Figure 4-4

Simplified Biological Model

(Used with Permission)

Signal propagation from the organ to the surface of the skin is influenced by factors such as the number of layers and the thickness, loss characteristics and temperature of each layer. Further, propagation is affected by reflections resulting from impedance changes at the boundaries between layers.

As a first approximation to the physiology of the human body, consider a similar structure with parallel planar layers consisting of fat and skin. The organ whose temperature is to be measured lies directly below the fat layer. The measurement is made

using radiometric emissions that have traveled vertically through the fat and skin layers and emerged into the ambient air above the skin layer. Since the material in each layer has its own complex permittivity, the attenuation, propagation and boundary reflection characteristics of the emission will change as the signal progresses ultimately to the ambient air. Additionally, each layer is assumed to have its own unique temperature (T). Figure 4-5 illustrates this concept.

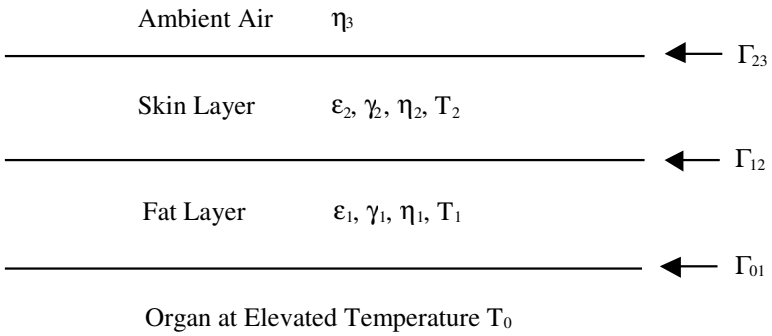

Figure 4-5

Two-Layer Biological Structure

Several assumptions are inherent in Figure 4-5. First, the boundary between the internal organ and the fat layer is assumed to be at temperature T_0 [58]. Secondly, the thickness of the ambient air layer is assumed to be negligible. This implies a receiving antenna that is proximal to, but not necessarily in contact with, the skin layer.

The internal organ at layer 0 emits electromagnetic radiation in accordance with equation 4-2 and corresponding to its elevated temperature in relation to the remaining

layers. As this radiation propagates through the fat and skin layers and into ambient air, the signal is affected by the propagation constants γ_1 and γ_2, the boundary reflection coefficients Γ_{12} and Γ_{23}, and the temperatures T_1 and T_2. Temperatures T1 and T2 are assigned values of 98.6°F and 80°F, and layer thicknesses L1 and L2 are 25 mm and 1 mm, respectively. Propagation through this structure is modeled using equations 4-11 and 4-12.

Losses L_1 and L_2 are implemented in the following manner. The propagation constant γ is a complex quantity with real and imaginary components α and β, respectively. Attenuation per unit length is represented by α, while β yields similar information for phase. Figure 2-3 shows the bulk attenuation as a function of frequency for select biological materials expressed in dB per mm. From this figure we obtain the information shown in Table 4-1 for skin and fat at 1.4 GHz.

Table 4-1

Propagation Constants for Skin and Fat at 1.4 GHz

Tissue	Attenuation (α)	Phase (β)
Dry Skin	0.2655 dB/mm	0.1873 rad/mm
Infiltrated Fat	0.0731 dB/mm	0.0983 rad/mm

The attenuation constants in Table 4-1 are converted to linear units for computational purposes using

$$Atten = 10^{\frac{-\alpha\ell}{10}} \quad , \tag{4-13}$$

where α is the attenuation constant from Table 4-1 and ℓ is the thickness of the respective layer in millimeters. The magnitude of the layer loss L is then calculated using the linear magnitude of the attenuation as a damping factor. We also account for the reflection losses (Γ_{12} and Γ_{23}) caused by impedances changes at the tissue boundaries. A MathCAD implementation of this code is given in Appendix F.

4.5 Results of Analysis

Figure 4-6 shows a plot of the calculated emitted structure temperature at 1.4 GHz, given a variable internal organ temperature. The internal temperature corresponds to a range of 98.3° to 103.7° F. The data shown in Figure 4-6 display linear characteristics similar to those of the power information in Figure 4-3, and demonstrate the utility of equations 4.11 and 4.12 for detecting diagnostically useful temperature changes within a biological structure.

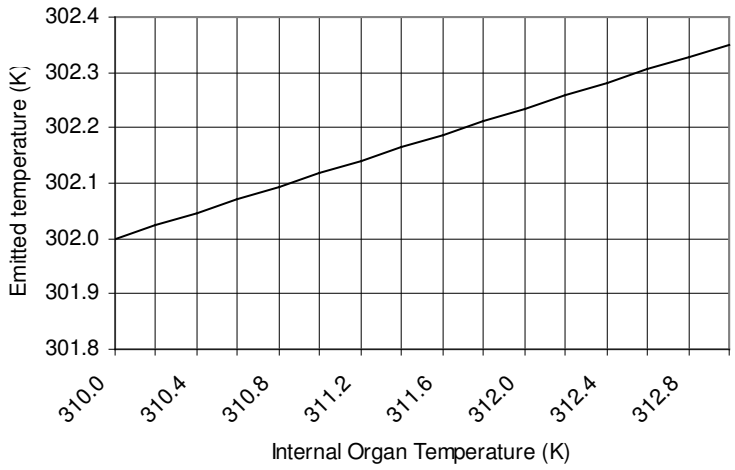

Figure 4-6

Emitted vs. Internal Temperatures for a Biological Structure

4.6 Verification

While the previous analysis demonstrates the working principle of equations 4.11 and 4.12, a more complex structure is needed to resonably approximate a typical human physiology. We constructed a physical model that could be used to generate experimental data and analyzed using these equations. This model consists of three layers: muscle, breast fat and skin in ascending order. We selected material phantoms with electrical properties corresponding as closely as possible to those of the respective biological materials in each layer. The phantoms included a hydroxyethylcellulose (HEC) solution for muscle, RANDO simulation material [59] for breast fat, and 93% lean ground beef for skin. Table 4-2 shows a comparison of the electrical properties of each phantom with the respective biological material.

Table 4-2

Permittivity Comparison for Biological Material Phantoms at 1.4 GHz

	HEC[1]	Muscle[2]	RANDO[1]	Breast Fat[2]	Beef[1]	Skin[2]
ε'	52.4159	54.1120	4.3950	5.3404	40.8768	39.7340
ε''	18.4890	14.6572	0.5800	0.9136	13.4560	13.5088

[1] Measured [2] Calculated using [10], [12]

A Total Power Radiometer (TPR) was designed and assembled to collect data from this construct. The TPR is based on information obtained from [60] and is described in Figure 4-7. Operation in the low GHz frequency range was determined to be suitable for this study; sensing depths would be on the order of 9 cm into adipose tissue and 2.4 cm into internal organs [61]. The specific operating frequency of 1.4 GHz was chosen to coincide with a radioastronomical "quiet" portion of the electromagnetic spectrum, in order to minimize the effect of external RF signals.

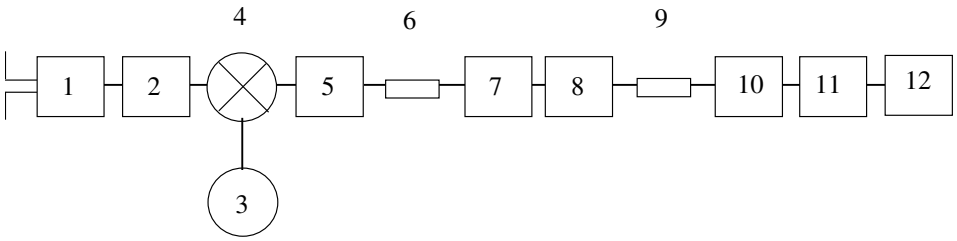

Component Descriptions:

1.) Low-Noise RF Amplifier, Gain = 34 dB, Noise Figure (NF) = 0.74 dB at 1.4 GHz
2.) Band-Pass Filter, 0.91 to 3 GHz, NF = 1.97 dB at 1.4 GHz
3.) Local Oscillator, Frequency = 1.1 GHz, Power = +8dBm
4.) Mixer, Conversion Loss = 7.5 dB, IF = 300 MHz
5.) Low-Noise IF Amplifier, Gain = 21 dB, NF = 0.8 dB at 300 MHz
6.) DC Block
7.) Low-Pass Filter, DC to 490 MHz, NF = 0.67 dB at 300 MHz
8.) Low-Noise IF Amplifier, Gain = 21 dB, NF = 0.8 dB at 300 MHz
9.) Diode Detector, 0.01 to 20 GHz, Sensitivity = 500 mV/mW
10.) DC Amplifier, DC to 17 MHz, Gain = 30 dB
11.) Low-Pass Filter, DC to 22 MHz
12.) Digital Millivoltmeter

Figure 4-7

Total Power Radiometer Block Diagram

The radiometer antenna, pictured to the left of the low noise RF amplifier in Figure 4-7, is a printed dipole designed for 1.4 GHz operation and has a practical bandwidth of approximately 300 MHz [60]. The antenna, along with its SMA-series input connector, is shown in Figure 4-8; the antenna frequency response curve is shown in Figure 4-9.

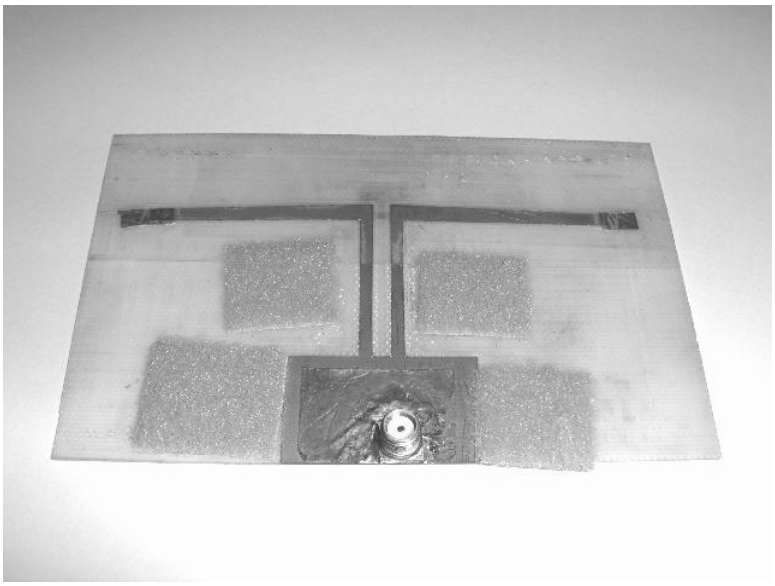

Figure 4-8

Total Power Radiometer Antenna

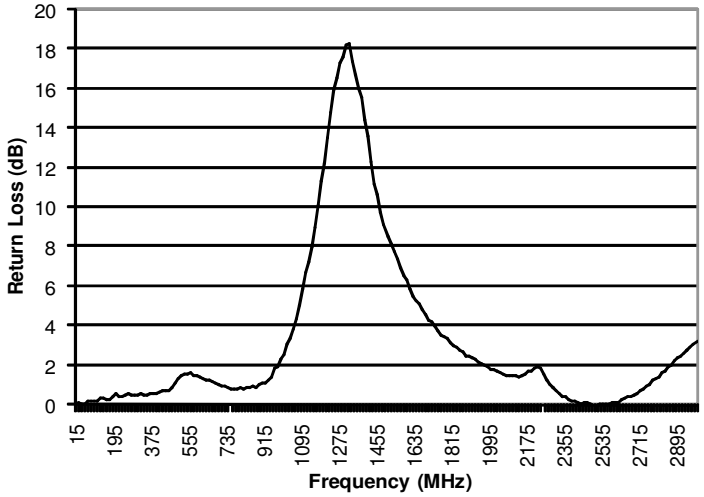

Figure 4-9

TPR Antenna Frequency Response

In order to mathematically accommodate this three-layered biological model, equations 4.11 and 4.12 are expanded to include a second intermediate temperature, resulting in

$$T_E = T_H'' / L_3 + T_3 (1 - 1/ L_3) \quad , \quad (4\text{-}14)$$

where T_H'' is given by

$$T_H'' = T_H' / L_2 + T_2(1 - 1/ L_2) \quad , \quad (4\text{-}15)$$

T_H' is defined as

$$T_H' = T_H / L_1 + T_1(1 - 1/ L_1) \quad , \quad (4\text{-}16)$$

and

L_1, L_2 and L_3 are the losses introduced by layers 1, 2 and 3, respectively. Implementation of this set of equations follows that of the two-layered model described previously.

An electrically quiet heat source is needed in order to establish a thermal gradient within the phantom construct, while emitting no RF noise outside that resulting from thermal emission. After some experimentation, we chose a reservoir of pre-heated water

for this task. The water serves as the internal organ at elevated temperature and provides initial temperature T_0 for analysis. It is the water temperature that is ultimately sensed by the radiometer system.

Rather than implementing a phantom construct whose physical dimensions would mimic those of an anatomical system, we constructed a model with dimensions that could be easily obtained and controlled using the phantom materials available. This decision was made in order to allow us to accurately analyze the test data and compare those results with those of our analyses. The layer thicknesses were:

HEC (muscle) = 3 mm

RANDO (fat) = 1 mm

Beef (skin) = 10 mm

Figure 4-10 shows a schematic diagram of the thermal test bed, including phantom layers and heat source.

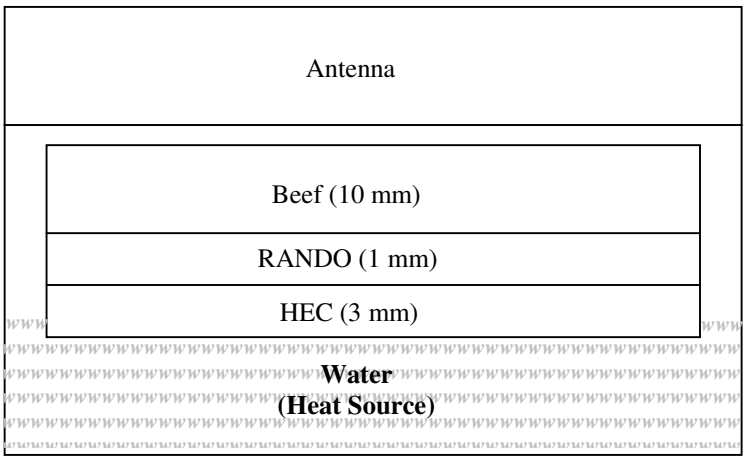

Figure 4-10

TPR Test Bed Schematic

The temperature at each phantom layer was monitored using a digital thermocouple. Additional temperatures monitored were those of the antenna and the hot and cold thermal references. A TTL logic-controlled switch installed between the antenna and the low noise RF amplifier determined the input to the radiometer. At each reading, the hot and cold reference temperatures and voltage levels were used to linearly interpolate the radiometric temperature corresponding to the antenna voltage. A schematic diagram of the switch configuration is shown in Figure 4-11.

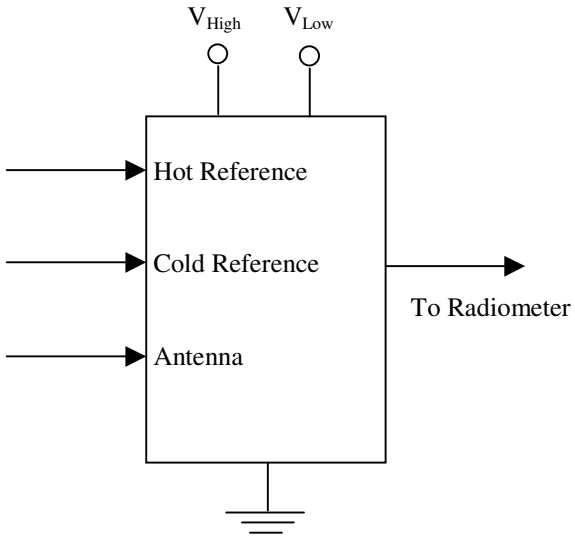

Figure 4-11

Input TTL Switch Configuration

We accounted for gain variations in the radiometer components by performing separate temperature calibrations at each data point, using the noise voltages emitted by the hot and cold references. The cold reference consisted of a 50 ohm resistor at a known temperature. The noise voltage corresponding to this temperature (approximately ambient) established one data point for linear interpolation. The hot reference was comprised of a calibrated noise source followed by a 20 dB attenuator. The noise source voltage, attenuated by the 20 dB pad at known temperature, established the second data point for linear interpolation. Depending on the attenuator temperature, the hot noise source voltage corresponded to approximately 390K (472°F).

Temperature and voltage information were taken as the pre-heated water cooled. Readings were taken at source temperature changes of 5° Fahrenheit; this scale was chosen because of its smaller temperature divisions compared to those of the Celsius scale. The readings taken were:

Water (organ) temperature

HEC (muscle) temperature

RANDO (fat) temperature

Beef (skin) temperature

Antenna temperature

Cold reference voltage

Hot reference voltage

Antenna (emission) voltage

Additionally, the physical temperatures of the hot and cold references were monitored throughout the data collection procedure. These data, in addition to those provided in Table 4-2 for the phantoms, were used by the MathCAD implementation of equations 4-14 through 4-16, as exemplified by the file shown in Appendix F.

A comparison of the test and analysis results is shown in Figure 4-12. The curves show a relatively constant temperature difference of 4K to 6K between the analysis and test results. This difference becomes more constant as the water temperature approaches

the values that may be encountered in a physiological application (≈ 310K to 313K). We attribute this phenomenon at least partly to the fact that the time rate of water cooling slows as the water temperature approaches that of its surroundings; this slower rate of cooling provides a more thermally stable phantom construct and allows for more accurate data collection.

The error bars attached to the solid curve (measured data) show the results of a Monte Carlo analysis performed to account for non-homogeneities in the skin phantom. Permittivity measurements taken at various points on and within the beef sample showed a range of complex values between approximately $(37.2 - j7.4)$ and $(53.2 - j23.4)$. A Monte Carlo simulation was executed in Advanced Design System (ADS) 2004A, in which the permittivity of the beef layer was allowed to uniformly vary between these extremes for 10,000 iterations. The change in received power was converted to temperature and represents the height of the error bars. This addition to Figure 4-10 allows us to show that the data agree within the limits of the permittivity uncertainty.

A fairly uniform offset exists between the curves, with the measured temperature being consistently lower than that calculated based on the propagation model. This offset may be attributed to a number of factors, including but not limited to antenna sidelobe effects, phantom non-homogeneity and the limitation of reflection effects (especially at the air-beef interface) to the first order. However, we are encouraged by the similarities in magnitude and average slope of the two curves, and offer these results as a

demonstration of the validity of our radiometric model for measuring internal body temperatures.

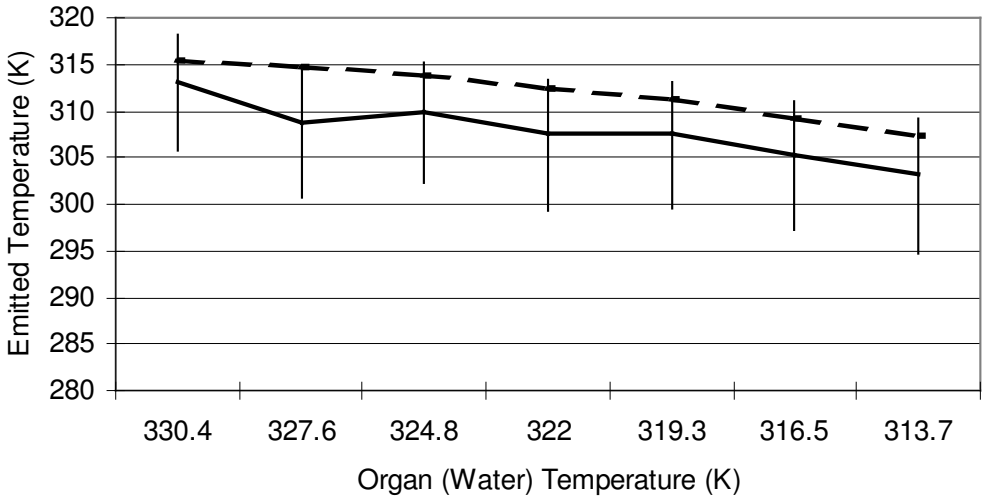

Figure 4-12

Radiometric Temperature of a Biological Phantom Construct

(Measured Temperature Solid, Calculated Temperature Dashed)

4.7 Measurement Sensitivity

While the material data available from [10] provide a reasonable estimate of the properties of biological tissue, they cannot supply the user with an estimate of the possible variations from person to person, or within the same person over time. For example, interpersonal variations in skin layer properties may result from factors such as pigmentation, moisture content, thickness, etc. [62]. Additionally, space flight has the potential to induce changes in fat content, bone density, muscle mass and other effects

within the same person during an extended mission [63]. A consideration of the effect these changes may have on the accuracy of radiometric measurements will provide insight into the ultimate utility of this technique to provide useful multi-personal data over extended periods of time.

We examined several parameters from an analytical standpoint for their effect on the emitted radiometric temperature from the body. Skin permittivity could easily vary from person to person, therefore we investigated the effect of permittivity changes on temperature emission. Table 4-2 lists typical complex skin permittivity at 1.4 GHz as approximately (40 – j14). We varied this value from (30 – j6) to (50 – j16) and compared the results with those of an analytical model that used the nominal value. The results, shown in Figure 4-13, indicate a rather pronounced effect on emitted temperature throughout the biological temperature range of 310K to 313K (98.3°F to 103.7°F). These results indicate the need for sensor calibration for each user.

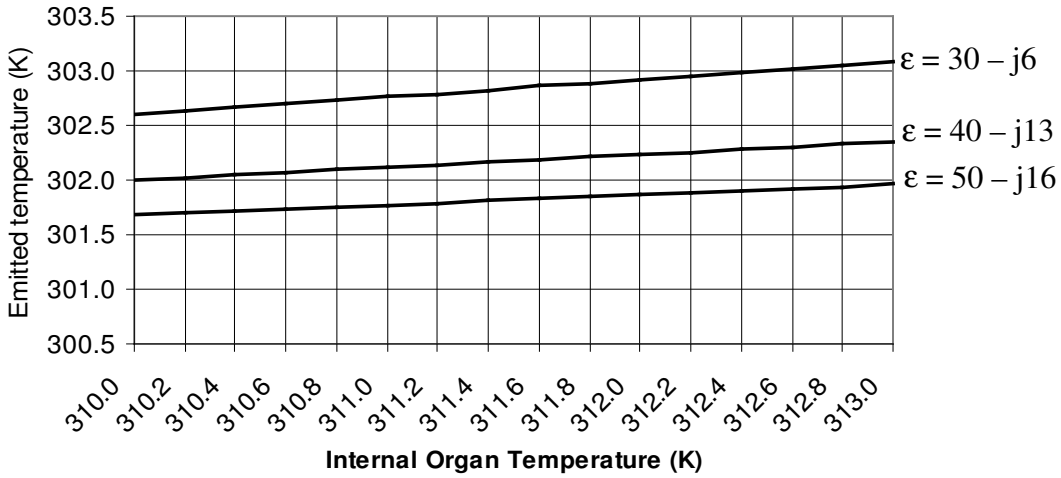

Figure 4-13

Effect of Skin Permittivity Variations on Emitted Temperature

We also examined the effect that a change in fat content might have on the measured temperature. For the purpose of our analysis, we modeled a fat content change as a difference in fat layer thickness, as might develop over time on an extended mission. Figure 4-14 shows the effect of a fat layer change on emitted temperature, as the layer thickness decreases from 25 mm to 5 mm. Normal body temperature (37°C, or 310.15K) is assumed in the model. The results show that, at elevated organ temperatures, a decrease in body fat thickness increases the sensitivity of the radiometric measurement. These results highlight the need for periodic calibration of the measuring system, to account for body parameter changes on extended missions.

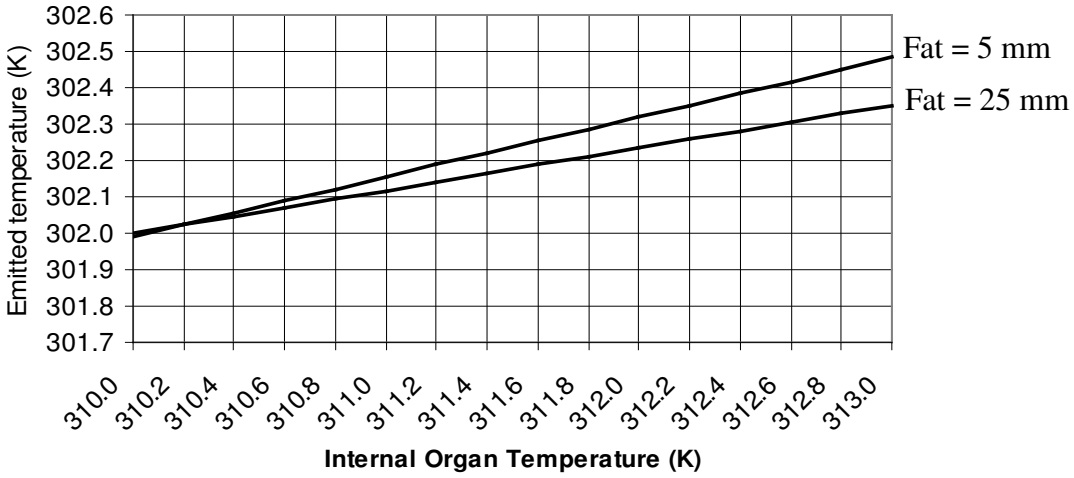

Figure 4-14

Effect of Fat Thickness Variations on Emitted Temperature

4.8 Limitations of Present Study

Several factors in the radiometer and model design and implementation contribute to the discrepancies noted between the measured and analytical temperatures in Figure 4-10. Some of the major limitations include:

The radiometer sensitivity, which is limited by (among other things) component noise factors. The present radiometer is constructed using commercial off-the-shelf (COTS) components that are not necessarily designed for radiometric use. For example, the stability of our present output in millivolts is limited to two decimal places. A time-averaging algorithm, while slowing the measurement speed, would improve the stability of the readings.

The diode detector sensitivity, which is assumed to be linear (at least in the temperature range of 310K to 313K). Any non-linearity in the diode response needs to be characterized, and our interpolation methods modified to accommodate this characterization.

The analytical model we are using, which does not account for system effects such as antenna pattern, efficiency and sidelobes, and losses within the measurement system.

4.9 Future Work

Much needs to be accomplished in order to fully demonstrate the applicability of this technique to a clinical or mission environment. The sensitivity of the radiometer must be increased to meet the goal of 0.02K measurement resolution. This may be accomplished by implementing more spohisticated radiometer designs, such as the Dicke radiometer [64]. The noise characteristics of the radiometer system and the environment require more rigorous definition than in the present work. Phantom selection needs to be based more closely on the biological materials being simulated. Finally, clinical tests need to be devised and implemented in order to fully determine the effectiveness of this technology.

4.9 Conclusion

Although research into the use of microwave radiometry for passive monitoring of internal conditions is in its relative infancy, this area nonetheless hold promises for multiple life-monitoring and potentially life-saving functions. Continuous non-contact evaluation of astronaut internal temperatures has already been discussed. Other potential applications of this technology include bone density loss detection, muscle mass measurements, and monitoring of cardiac function [66]. These functions have significant implication for terrestrial uses, as well.

Chapter 5

Summary and Conclusion

5.1 Summary

In this work we have investigated several potential new applications of microwave radiometry for the biomedical field. It may certainly be said that the basic technologies presented in the previous chapters are not new or original. The innovation lies in the context of the applications for which these techniques have been investigated and adapted.

For example, we are unaware of any past or contemporary research efforts being made toward the detection of blood oxygen resonances near 60 GHz. The impetus for this direction was provided in no small part by our participation in the NSF IGERT SKINS fellowship at the University of South Florida, which encouraged research into the nature of skin as an interface for internal physiological phenomena.

Our work on radiometric techniques for the measurement of internal body temperatures was inspired not only by the goals of the IGERT fellowship, but also by our fascination with and support of the exploration of space. It is our hope that this

innovative, continuous and non-invasive method of health monitoring may contribute in some small way to mankind's continuation and expansion, while at the same time adding to the quality of life here on Earth.

5.2 Conclusion

The progress of mankind has for centuries been driven in no small part by a need to explore its environment. Whether that environment is external, such as land, sea, air and space, or internal in the case of the human body and mind, the need for knowledge through exploration has and will continue to help define the species as it is. For the hope that this work may contribute in some small way to this spirit of exploration, we are extremely grateful.

List of References

[1] Brussaard, G. and Watson, P.A., "Atmospheric Modelling and Millimetre Wave Propagation" Chapman and Hall, 1995, ch. 1, pp. 10-15.

[2] Ulaby, F.T., Moore, R.K. and Fung, A.K., "Microwave Remote Sensing, Active and Passive" Artech House, 1981, vol. 1, ch. 5, pp. 274-279.

[3] Stimson, G.W., "Introduction to Airborne Radar" Hughes Aircraft Company, 1983, ch. 7, p.125.

[4] Rogacheva, S., Kuznetsov, P., Popyhova, E. and Somov, A., "Metronidazole Protects Cells from Microwaves" International Society for Optical Engineering, 2006, www.newsroom.spie.org/x5111.xml.

[5] Pozar, D.M., "Microwave Engineering" (3rd ed.) John Wiley and Sons, 2005, ch. 1, p. 29.

[6] Brussaard, G. and Watson, P.A., "Atmospheric Modelling and Millimetre Wave Propagation" Chapman and Hall, 1995, ch. 1, pp. 10-15.

[7] Ulaby, F.T., Moore, R.K. and Fung, A.K., "Microwave Remote Sensing, Active and Passive" Artech House, 1981, vol. 1, ch. 5, pp. 264-266.

[8] Ulaby, F.T., Moore, R.K. and Fung, A.K., "Microwave Remote Sensing, Active and Passive" Artech House, 1981, vol. 1, ch. 4, pp. 192-194.

[9] Vander Vorst, A., Rosen, A. and Kotsuka, Y., "RF/Microwave Interaction with Biological Tissues" IEEE Press/Wiley-Interscience, 2006, ch. 1, p. 19.

[10] Gabriel, C. and Gabriel, S., "Compilation of the Dielectric Properties of Body Tissues at RF and Microwave Frequencies" Brooks AFB report number AL/OE-TR-1996-0037.

[11] Cole, K.S. and Cole, R.H., "Dispersion and Absorption in Dielectrics. I. Alternating Current Characteristics" Journal of Chemistry and Physics, 1941, vol. 9, pp. 341-351.

[12] Anderson, V. and Rowley, J. (compilers), "Tissue Dielectric Properties Calculator" Telstra Research Laboratories, 1998, www.swin.edu.au/bsee/maz/webpage/tissues3.xls.

[13] Balanis, C.A., "Advanced Engineering Electromagnetics" John Wiley and Sons, 1989, ch. 1, p.7.

[14] Brussaard, G. and Watson, P.A., "Atmospheric Modelling and Millimetre Wave Propagation" Chapman and Hall, 1995, ch. 2, p. 29-32.

[15] Ulaby, F.T., Moore, R.K. and Fung, A.K., "Microwave Remote Sensing, Active and Passive" Artech House, 1981, vol. 1, ch. 5, pp. 274-277.

[16] Brussaard, G. and Watson, P.A., "Atmospheric Modelling and Millimetre Wave Propagation" Chapman and Hall, 1995, ch. 2, pp. 13-15.

[17] Brussaard, G. and Watson, P.A., "Atmospheric Modelling and Millimetre Wave Propagation" Chapman and Hall, 1995, ch. 2, p. 31.

[18] Ulaby, F.T., Moore, R.K. and Fung, A.K., "Microwave Remote Sensing, Active and Passive" Artech House, 1981, vol. 1, ch. 5, p. 278.

[19] Bueche, F.J., Schaum's Outline Series, "Theory and Problems of College Physics" (7^{th} ed.) McGraw-Hill, Inc., 1979, ch. 16, p. 123.

[20] West, J.B., "Respiratory Physiology – The Essentials" (2^{nd} ed.) Williams and Wilkins, 1979, ch. 1, p. 1-2.

[21] West, J.B., "Respiratory Physiology – The Essentials" (2^{nd} ed.) Williams and Wilkins, 1979, ch. 5, p. 52.

[22] West, J.B., "Respiratory Physiology – The Essentials" (2^{nd} ed.) Williams and Wilkins, 1979, ch. 3, p. 25.

[23] Shapiro, B.A., Harrison, R.A. and Walton, J.R., "Clinical Application of Blood Gasses" (3^{rd} ed.) Year Book Medical Publishers, 1982, ch. 1, p. 8.

[24] Brussaard, G. and Watson, P.A., "Atmospheric Modelling and Millimetre Wave Propagation" Chapman and Hall, 1995, ch. 2, p. 29.

[25] Shapiro, B.A., Harrison, R.A. and Walton, J.R., "Clinical Application of Blood Gasses" (3^{rd} ed.) Year Book Medical Publishers, 1982, ch. 14, p. 155.

[26] Shapiro, B.A., Harrison, R.A. and Walton, J.R., "Clinical Application of Blood Gasses" (3rd ed.) Year Book Medical Publishers, 1982, ch. 14, p. 156.

[27] Rapid QC© Complete Level 1, 2, 3 Data Sheet, Bayer Healthcare LLC, 2003.

[28] "Lightning™ Network Analysis Solutions for Design and Manufacturing" Anritsu Company, 2007.

[29] Kleinsmith, L.J., Kerrigan, D., Kelly, J., and Hollen, B., "Understanding Angiogenesis" National Cancer Institute, http://cancer.gov/cancertopics/understandingcancer/angiogenesis.

[30] Freinkel, R.K. and Woodley, D.T. eds., "The Biology of the Skin" Parthenon Publishing Group, 2001, chap. 21, p. 341.

[31] The Skin Cancer Foundation, "Skin Cancer Facts", www.skincancer.org/skincancer-facts.php.

[32] MelanomaCenter.org, http://www.melanomacenter.org/staging/tnmstagingsystem.html

[33] King, D., "Introduction to Skin Histology" Southern Illinois School of Medicine, 2006, http://www.siumed.edu/~dking2/intro/skin.htm.

[34] Revis, D.R. Jr. and Seagle, M.B., "Skin Anatomy" emedicine.com, 2006, http//www.emedicine.com/plastic/topic389.htm

[35] MelanomaCenter.org, http://www.melanomacenter.org/basics/melanomas.html

[36] Beetner, D.G., Kapoor, S., Manjunath, S., Zhou, X. and Stoecker, W.V., "Differentiation Among Basal Cell Carcinoma, Benign Lesions, and Normal Skin Using Electric Impedance" IEEE Transactions on Biomedical Engineering, August 2003, pp. 1020-1025.

[37] Åberg, P., Nicander, I., Holmgren, U., Geladi, P. and Ollmar, S., "Assessment of Skin Lesions and Skin Cancer using Simple Electrical Impedance Indices" Skin Research and Technology, 2003, vol. 9, pp. 257-261.

[38] Mehrübeoğlu, M., Kehtmavaz, N., Marquez, G., Duvic, M. and Wang, L.V., "Skin Lesion Classification Using Oblique-Incidence Diffuse Reflectance Spectroscopic Imaging" Applied Optics, January 2002, pp. 182-192.

[39] Cui, W., Ostrander, L.E. and Lee, B.Y., "In Vivo Reflectance of Blood and Tissue as a Function of Light Wavelength" IEEE Transactions on Biomedical Engineering, June 1990, pp. 632-639.

[40] Berardesca, E., Elsner, P. and Maibach, H.I., eds., "Bioengineering of the Skin, Cutaneous Blood Flow and Erythema" CRC Press, 1995, ch. 8, p. 123.

[41] Ulaby, F.T., Moore, R.K. and Fung, A.K., "Microwave Remote Sensing, Active and Passive" Artech House, 1981, vol. 1, ch. 6, p. 345.

[42] Bigu del Bianco, J., Romero-Sierra, C. and Tanner, J.A., "Some Theory and Experiments on Microwave Radiometry of Biological Systems" S-MTT Microwave Symposium Digest, June 1974, pp. 41-44.

[43] Bardati, F., Mongiardo, M., Solimini, D. and Tognolatti, P., "Biological Temperature Retrieval by Scanning Radiometry" IEEE MTT-S International Microwave Symposium Digest, June 1986, pp. 763-766.

[44] Carr, K.L., "Microwave Radiometry: Its Importance to the Detection of Cancer" IEEE Transactions on Microwave Theory and Techniques, December 1989, pp. 1862-1869.

[45] Carr, K.L., "Radiometric Sensing" IEEE Potentials, April/May 1997, pp. 21-25.

[46] Land, D.V., "Medical Microwave Radiometry and its Clinical Applications" IEE Colloquium on the Application of Microwaves in Medicine, February 1995, pp. 2/1-2/5.

[47] Ulaby, F.T., Moore, R.K. and Fung, A.K., "Microwave Remote Sensing, Active and Passive" Artech House, 1981, vol. 1, ch. 4, p. 192.

[48] Ulaby, F.T., Moore, R.K. and Fung, A.K., "Microwave Remote Sensing, Active and Passive" Artech House, 1981, vol. 1, ch. 4, p. 198.

[49] Ulaby, F.T., Moore, R.K. and Fung, A.K., "Microwave Remote Sensing, Active and Passive" Artech House, 1981, vol. 1, ch. 4, p. 200.

[50] Wilheit, T.T. Jr., "Radiative Transfer in a Plane Stratified Dielectric" IEEE Transactions on Geoscience Electronics, April 1978, pp. 138-143.

[51] Ulaby, F.T., Moore, R.K. and Fung, A.K., "Microwave Remote Sensing, Active and Passive" Artech House, 1981, vol. 1, ch. 4, pp. 232-245.

[52] Montreuil, J. and Nachman, M., "Multiangle Method for Temperature Measurement of Biological Tissues by Microwave Radiometry" IEEE Transactions on Microwave Theory and Technoques, July 1991, pp. 1235-1239.

[53] Ulaby, F.T., Moore, R.K. and Fung, A.K., "Microwave Remote Sensing, Active and Passive" Artech House, 1981, vol. 1, ch. 6, p. 349.

[54] Pozar, D.M., "Microwave Engineering" (3rd ed.) John Wiley and Sons, 2005, ch. 10, p. 494.

[55] Roeder, R., Raytheon Company, "Simple Model" electronic correspondence to T. Weller at University of South Florida, August 2006.

[56] Cheever, E.A. and Foster, K.R., "Microwave Radiometry in Living Tissue: What Does it Measure?" IEEE Transactions on Biomedical Engineering, June 1992, pp. 563-568.

[57] The Phantom Laboratory, Salem NY, http://www.phantomlab.com/rando.html

[58] Ulaby, F.T., Moore, R.K. and Fung, A.K., "Microwave Remote Sensing, Active and Passive" Artech House, 1981, vol. 1, ch. 6, pp. 360-367.

[59] Bonds, Q., Weller, T., Maxwell, E., Ricard, T., Odu, E. and Roeder, R., "The Design and Analysis of a Total Power Radiometer (TPR) for Non-Contact Biomedical Sensing Applications" (unpublished manuscript) University of South Florida, February 2008.

[60] Vander Vorst, A., Rosen, A. and Kotsuka, Y., "RF/Microwave Interaction with Biological Tissues" IEEE Press/Wiley-Interscience, 2006, ch. 2, pp. 69-82.

[61] Roeder, B., Weller, T., and Harrow, J., "Technical Proposal for Astronaut Health Monitoring Using a Microwave Free-Space Sensor" (Preliminary) University of South Florida and Raytheon Company, December 2007, p. 13.

[62] Ulaby, F.T., Moore, R.K. and Fung, A.K., "Microwave Remote Sensing, Active and Passive" Artech House, 1981, vol. 1, ch. 6, pp. 369-374.

[63] Roeder, B., Weller, T., and Harrow, J., "Technical Proposal for Astronaut Health Monitoring Using a Microwave Free-Space Sensor" (Preliminary) University of South Florida and Raytheon Company, December 2007, p. 14.

Appendices

Appendix A Electrical Properties of Various Biological Materials

The properties of complex permittivity, conductivity, and attenuation are shown in Figures 2-1 through 2-3 for tissues and organs of specific interest to this work. The corresponding properties of the following tissues and organs are contained in this Appendix, for reference and completeness:

Cartilage

Cortical Bone

Cancellous Bone

Infiltrated Bone Marrow

Cortical bone refers to the hard, outer portion of bony tissue. Cancellous bone indicates the relatively soft, spongy interior tissue which allows space for blood vessels and marrow. Infiltrated bone marrow refers to marrow containing other related tissue, such as blood vessels.

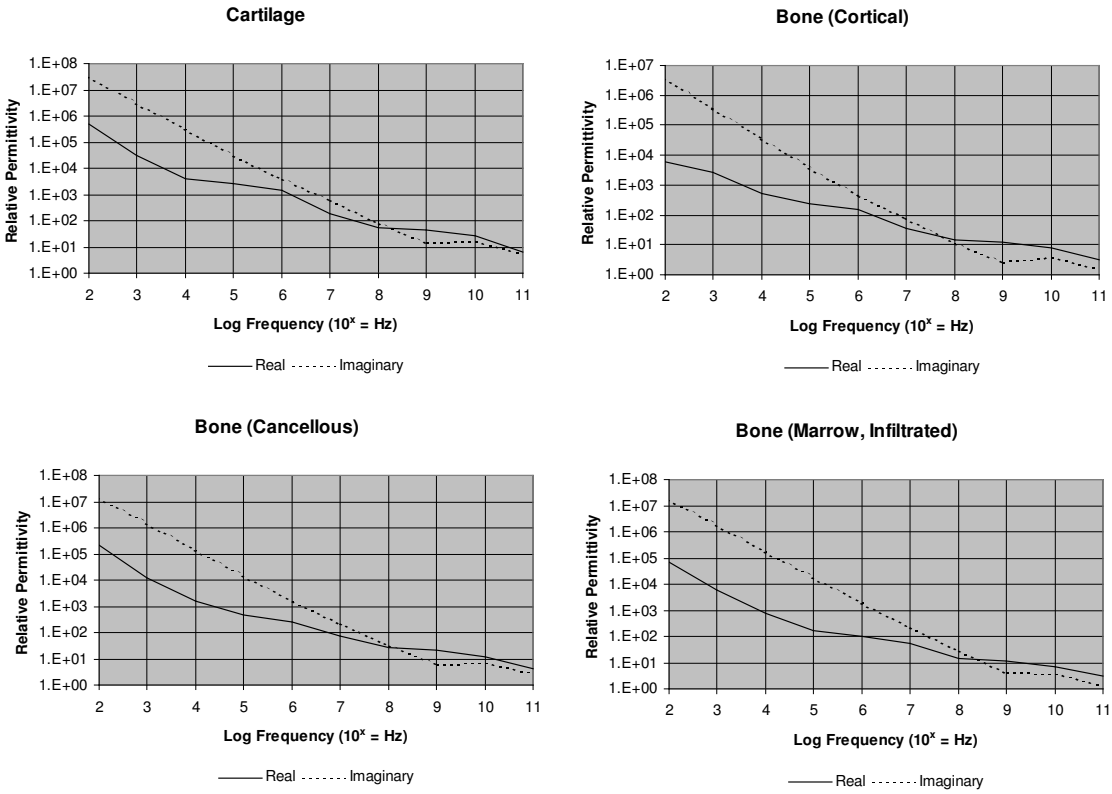

Figure A-1

Complex Permittivity of Various Biological Materials

Appendix A (Continued)

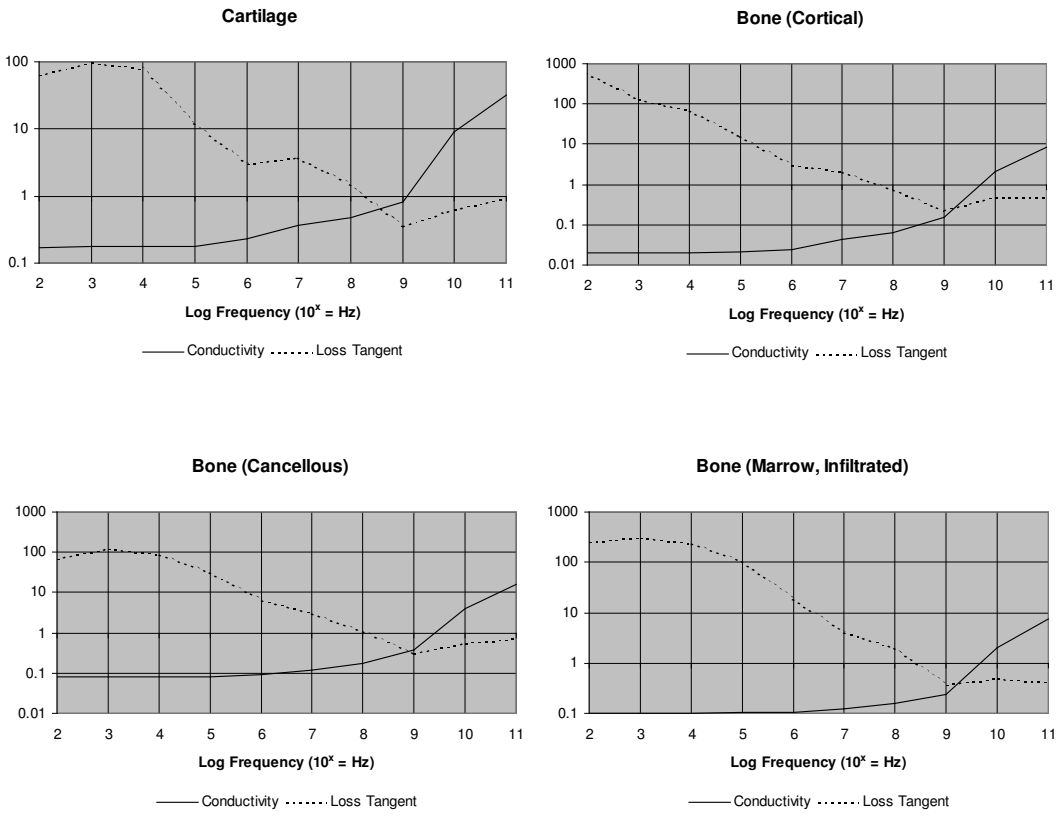

Figure A-2

Conductivity and Loss Tangent of Various Biological Materials

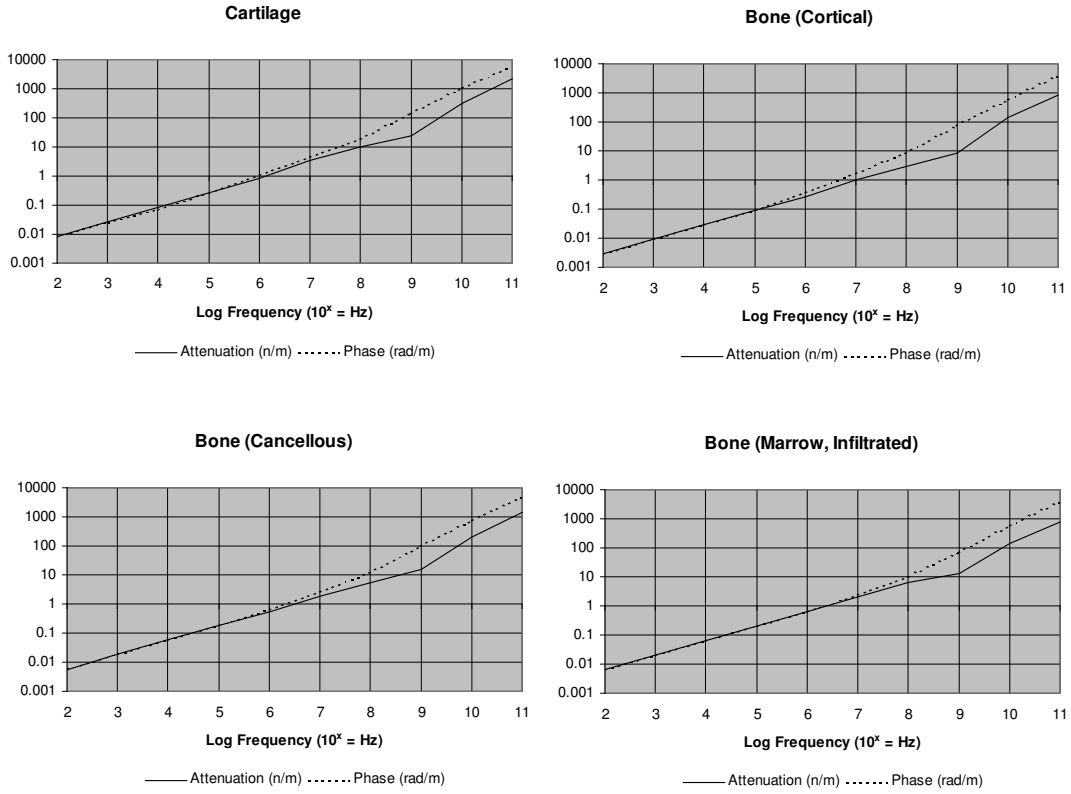

Figure A-3

Attenuation and Phase Characteristics of Various Biological Materials

Appendix B MATLAB Code for Oxygen Resonance by Reduced Line Base Method

```
%
%   Oxygen Attenuation Calculator
%
%   Based on Brussard & Watson,
%   "Atmospheric Modelling and Millimetre Wave Propagation"
%   and using the Reduced Line Base Model of Liebe
%
%   Version 2, July 22, 2006
%  (Version 1 was lost due to hard drive failure)
%
%   Spectral Line Coefficients:
%
%   f = Spectral Line Frequency in GHz
%
f = [51.5034 52.0214 52.5424 53.0669 53.5957 54.1300 54.6712 55.2214 ...
    55.7838 56.2648 56.3634 56.9682 57.6125 58.3269 58.4466 59.1642 ...
    59.5910 60.3061 60.4348 61.1506 61.8002 62.4112 62.4863 62.9980 ...
    63.5685 64.1278 64.6789 65.2241 65.7648 66.3021 66.8368 67.3696 ...
    67.9009];
%
%   a1 = Spectral Line Strength Factor (*E-7 KHz per millibar)
%
a1 = [6.08 14.14 31.02 64.1 124.7 228.0 391.8 631.6 953.5 548.9 1344 ...
    1763 2141 2386 1457 2404 2112 2124 2461 2504 2298 1933 1517 1503 ...
    1087 733.5 463.5 274.8 153.0 80.09 39.46 18.32 8.01];
%
a1 = a1*10^(-7);
%
%   a2 = Spectral Line Strength Temperature Dependency
%
a2 = [7.74 6.84 6.00 5.22 4.48 3.81 3.19 2.62 2.12 0.01 1.66 1.26 0.91 ...
    0.62 0.08 0.39 0.21 0.21 0.39 0.62 0.91 1.26 0.08 1.66 2.11 2.62 ...
    3.19 3.81 4.48 5.22 6.00 6.84 7.74];
%
%   a3 = Spectral Line Width Factor (*E-4 GHz per millibar)
%
a3 = [8.90 9.20 9.40 9.70 10.00 10.20 10.50 10.79 11.10 16.46 11.44 ...
    11.81 12.21 12.66 14.49 13.19 13.60 13.82 12.97 12.48 12.07 11.71 ...
    14.68 11.39 11.08 10.78 10.50 10.20 10.00 9.70 9.40 9.20 8.90];
%
a3 = a3*10^(-4);
%
```

Appendix B (Continued)

```
%   a4 = Spectral Line Interference Factor (*E-4 per millibar)
%
a4 = [5.60 5.50 5.70 5.30 5.40 4.80 4.80 4.17 3.75 7.74 2.97 2.12 0.94 ...
   -0.55 5.97 -2.44 3.44 -4.13 1.32 -0.36 -1.59 -2.66 -4.77 -3.34 ...
   -4.17 -4.48 -5.10 -5.10 -5.70 -5.50 -5.90 -5.60 -5.80];
%
a4 = a4*10^(-4);
%
%   a5 = Spectral Line Interference Temperature Dependency
%
a5 = [1.8 1.8 1.8 1.9 1.8 2.0 1.9 2.1 2.1 0.9 2.3 2.5 3.7 -3.1 0.8 0.1 ...
   0.5 0.7 -1.0 5.8 2.9 2.3 0.9 2.2 2.0 2.0 1.8 1.9 1.8 1.8 1.7 1.8 1.7];
%
%   Pressure and Temperature Parameters
%
%   p = dry air pressure in millibars (1013.3 mbar = 1 atm.)
%   e = water vapor partial pressure in millibars
%   T = temperature in Kelvin
%   freq = computation frequency in GHz
%
p = 212.73  %   Atmospheric pO2
e = 9.45    %   Value in Air
T = 291.15  %   Lab Air Temp
t = 300/T
count = 1;
for freq = 50:0.0375:65;
%
%   Wet Continuum
%
Nw = 1.18*10^(-8)*(p+30.3*e*t^6.2)*freq*e*t^3.0 + ...
   2.3*10^(-10)*p*e^1.1*t^2*freq^1.5;
%
%   Dry Continuum
%
d = 5.6*10^(-4)*(p+1.1*e)*t^0.8;
%
Nd = (freq*p*t^2)*(6.14*10^(-5)/(d*(1+(freq/d)^2)*(1+(freq/60)^2)) + ...
   1.4*10^(-11)*(1-1.2*10^(-5)*freq^1.5)*p*t^1.5);
%
%   Spectral Line Interference
%
```

Appendix B (Continued)

```
s = a4.*p.*t.^(a5);
%
%   Spectral Line Width
%
deltaf = a3*(p*t^0.8+1.1*e*t);
%
%   Line Shape Factor
%
F = (freq./f).*((deltaf-s.*(f-freq))./((f-freq).*(f-freq)+deltaf.*deltaf) + ...
   (deltaf-s.*(f+freq))./((f+freq).*(f+freq)+deltaf.*deltaf));
%
%   Line Strength
%
S = a1.*p*t^3.*exp(1).^(a2.*(1-t));
%
%   Imaginary Part of Complex Refractivity
%
Ndoubleprime = sum(S.*F) + Nd + Nw;
%
%   Gaseous Absorption Coefficient in dB per Kilometer
%
alpha(count) = 0.1820*freq*Ndoubleprime;
count = count + 1;
end
```

Appendix C MATLAB Code for Oxygen Resonance by Theory of Overlapping Lines

```
%
%   Oxygen Attenuation Calculator
%
%   Based on Ulaby, Moore & Fung,
%   "Microwave Remote Sensing, Active and Passive (Volume 1)"
%   and using the Theory of Overlapping Lines of Rosenkrantz (1975)
%
%   November 24, 2006
%
%   Input Tabulated Parameters
%
%   Rotational Quantum Numbers
%
N = [1 3 5 7 9 11 13 15 17 19 21 23 25 27 29 31 33 35 37 39];
%
%   Resonant Frequencies (GHz)
%
fNplus = [56.2648 58.4466 59.5910 60.4348 61.1506 61.8002 62.4112 ...
   62.9980 63.5685 64.1278 64.6789 65.2241 65.7647 66.3020 66.8367 ...
   67.3694 67.9007 68.4308 68.9601 69.4887];
%
fNminus = [118.7503 62.4863 60.3061 59.1642 58.3239 57.6125 56.9682 ...
   56.3634 55.7838 55.2214 54.6711 54.1300 53.5957 53.0668 52.5422 ...
   52.0212 51.5030 50.9873 50.4736 49.9618];
%
%   Interference Coefficients (per millibar)
%
YNplus = [4.51 4.94 3.52 1.86 0.33 -1.03 -2.23 -3.32 -4.32 -5.26 ...
   -6.13 -6.99 -7.74 -8.61 -9.11 -10.3 -9.87 -13.2 -7.07 -25.8];
YNplus = YNplus*10^(-4);
%
YNminus = [-0.214 -3.78 -3.92 -2.68 -1.13 0.344 1.65 2.84 3.91 ...
   4.93 5.84 6.76 7.55 8.47 9.01 10.3 9.86 13.3 7.01 26.4];
YNminus =  YNminus*10^(-4);
%
%   Input Conditional Variables
%
count = 0;
for f = 50:0.0375:65;    % Frequency in GHz
   count = count + 1;
P = 212.8    % Total pressure in millibars (1 atm = 1013 mb)
```

Appendix C (Continued)

```
T = 291     % Temperature in degrees Kelvin (300 K = 80 F)
%
%   Calculations
%
gammaN = 1.18*(P/1013)*(300/T)^0.85;    % Resonant Line width Parameters
gammab = 0.49*(P/1013)*(300/T)^0.89;    % Nonresonant Line width Parameters
%
%   Spectral Line Amplitudes
%
dNplus = sqrt(N.*(2*N+3)./((N+1).*(2*N+1)));
dNminus = sqrt((N+1).*(2*N-1)./(N.*(2*N+1)));
%
PhiN = 4.6*10^(-3)*(300/T)*(2*N+1).*exp((-6.89*10^(-3))*N.*(N+1)*(300/T));
%
gNplus_of_plus_f = ((gammaN*dNplus.*dNplus)+ ...
   P*(f-fNplus).*YNplus)./((f-fNplus).*(f-fNplus)+gammaN^2);
gNplus_of_minus_f = ((gammaN*dNplus.*dNplus)+ ...
   P*(-f-fNplus).*YNplus)./((-f-fNplus).*(-f-fNplus)+gammaN^2);
%
gNminus_of_plus_f = ((gammaN*dNminus.*dNminus)+ ...
   P*(f-fNminus).*YNminus)./((f-fNminus).*(f-fNminus)+gammaN^2);
gNminus_of_minus_f = ((gammaN*dNminus.*dNminus)+ ...
   P*(-f-fNminus).*YNminus)./((-f-fNminus).*(-f-fNminus)+gammaN^2);
%
%   Absorption Spectrum Shape
%
Fprime = ((0.7*gammab)/(f^2+gammab^2))+ ...
   sum(PhiN.*(gNplus_of_plus_f+gNplus_of_minus_f+ ...
   gNminus_of_plus_f+gNminus_of_minus_f));
%
%   Oxygen Absorption Coefficient
%
k(count) = 1.61*10^(-2)*f^2*(P/1013)*(300/T)^2*Fprime;
end
```

Appendix D Bovine Blood Permittivity Data

November 12, 2007 10:11 AM

Frequency (Hz)	e'	e"
50000000000.	11.3313	14.6332
50037500000.	11.3585	14.6593
50075000000.	11.3888	14.6613
50112500000.	11.4637	14.6939
50150000000.	11.5138	14.6356
50187500000.	11.5801	14.5406
50225000000.	11.6193	14.4618
50262500000.	11.6275	14.3224
50300000000.	11.4441	14.1143
50337500000.	11.3757	13.9545
50375000000.	11.2532	13.8260
50412500000.	11.1395	13.8145
50450000000.	11.0375	13.6864
50487500000.	10.9343	13.6788
50525000000.	10.8712	13.7540
50562500000.	10.7800	13.8081
50600000000.	10.7517	13.8986
50637500000.	10.7441	14.0085
50675000000.	10.7461	14.1385
50712500000.	10.7675	14.2108
50750000000.	10.8059	14.2932
50787500000.	10.8525	14.3444
50825000000.	10.9065	14.3416
50862500000.	10.9403	14.3263
50900000000.	11.0186	14.2417
50937500000.	11.0338	14.1359
50975000000.	11.0528	14.0449
51012500000.	10.9883	13.9757
51050000000.	10.9660	13.8068
51087500000.	10.8907	13.7523
51125000000.	10.7884	13.6670
51162500000.	10.7150	13.6515
51200000000.	10.6325	13.6269
51237500000.	10.5971	13.6500
51275000000.	10.5159	13.7196
51312500000.	10.4746	13.7752
51350000000.	10.4574	13.8402
51387500000.	10.4168	13.9480

Appendix D (Continued)

51425000000.	10.4444	14.0007
51462500000.	10.4898	14.0953
51500000000.	10.5139	14.1037
51537500000.	10.5726	14.0855
51575000000.	10.6237	14.0798
51612500000.	10.6620	14.0554
51650000000.	10.6716	13.9544
51687500000.	10.6768	13.8685
51725000000.	10.6898	13.7258
51762500000.	10.6391	13.6935
51800000000.	10.5891	13.5895
51837500000.	10.5039	13.5210
51875000000.	10.4481	13.5150
51912500000.	10.3889	13.4933
51950000000.	10.2973	13.5211
51987500000.	10.2531	13.5470
52025000000.	10.2213	13.5825
52062500000.	10.1969	13.6681
52100000000.	10.1872	13.7270
52137500000.	10.2021	13.7784
52175000000.	10.2245	13.8314
52212500000.	10.2738	13.8617
52250000000.	10.2972	13.8660
52287500000.	10.3069	13.8638
52325000000.	10.3473	13.8115
52362500000.	10.3880	13.7820
52400000000.	10.3887	13.6423
52437500000.	10.3578	13.5912
52475000000.	10.3508	13.5018
52512500000.	10.2713	13.4278
52550000000.	10.2418	13.3880
52587500000.	10.1817	13.3427
52625000000.	10.1315	13.3353
52662500000.	10.0672	13.3270
52700000000.	10.0204	13.3778
52737500000.	9.9804	13.4159
52775000000.	9.9748	13.4467
52812500000.	9.9506	13.5262
52850000000.	9.9467	13.5666
52887500000.	9.9786	13.6111
52925000000.	10.0055	13.6184
52962500000.	10.0490	13.6318

Appendix D (Continued)

53000000000.	10.0987	13.6006
53037500000.	10.1266	13.5468
53075000000.	10.1826	13.4902
53112500000.	10.1660	13.4260
53150000000.	10.1605	13.3564
53187500000.	10.1290	13.2616
53225000000.	10.0862	13.2247
53262500000.	10.0569	13.1614
53300000000.	10.0056	13.1100
53337500000.	9.9507	13.1399
53375000000.	9.9194	13.1155
53412500000.	9.8470	13.1519
53450000000.	9.8242	13.1916
53487500000.	9.8172	13.2255
53525000000.	9.7995	13.2830
53562500000.	9.8228	13.3093
53600000000.	9.8285	13.3413
53637500000.	9.8876	13.3651
53675000000.	9.8987	13.3823
53712500000.	9.9456	13.3728
53750000000.	9.9856	13.3166
53787500000.	10.0135	13.2885
53825000000.	10.0376	13.2160
53862500000.	10.0297	13.1535
53900000000.	9.9886	13.0567
53937500000.	9.9737	13.0320
53975000000.	9.9321	12.9546
54012500000.	9.8903	12.9403
54050000000.	9.8270	12.9194
54087500000.	9.7893	12.9218
54125000000.	9.7457	12.9347
54162500000.	9.7002	12.9906
54200000000.	9.6809	13.0143
54237500000.	9.6782	13.0616
54275000000.	9.6597	13.1101
54312500000.	9.6744	13.1188
54350000000.	9.7182	13.1539
54387500000.	9.7088	13.1792
54425000000.	9.7697	13.1313
54462500000.	9.7817	13.0840
54500000000.	9.8039	13.0310
54537500000.	9.8199	13.0020

Appendix D (Continued)

54575000000.	9.8108	12.9272
54612500000.	9.7893	12.8611
54650000000.	9.7580	12.7831
54687500000.	9.7239	12.7557
54725000000.	9.6796	12.7095
54762500000.	9.6331	12.6938
54800000000.	9.5774	12.6985
54837500000.	9.5467	12.7066
54875000000.	9.5071	12.7296
54912500000.	9.5006	12.7607
54950000000.	9.4780	12.8303
54987500000.	9.4968	12.8645
55025000000.	9.4837	12.8669
55062500000.	9.4783	12.8802
55100000000.	9.5151	12.8820
55137500000.	9.5190	12.8795
55175000000.	9.5682	12.8253
55212500000.	9.6152	12.8255
55250000000.	9.7036	12.8019
55287500000.	9.7650	12.8199
55325000000.	9.7926	12.8105
55362500000.	9.7619	12.7289
55400000000.	9.6387	12.6048
55437500000.	9.4495	12.4744
55475000000.	9.3620	12.4503
55512500000.	9.3142	12.4256
55550000000.	9.3046	12.4711
55587500000.	9.2471	12.4557
55625000000.	9.2886	12.5333
55662500000.	9.2730	12.5397
55700000000.	9.2857	12.5939
55737500000.	9.3365	12.6471
55775000000.	9.3395	12.6728
55812500000.	9.4132	12.6718
55850000000.	9.3491	12.6034
55887500000.	9.5683	12.7419
55925000000.	9.5062	12.6209
55962500000.	9.5341	12.5530
56000000000.	9.5592	12.5366
56037500000.	9.5069	12.4691
56075000000.	9.4227	12.3235
56112500000.	9.3297	12.2506

Appendix D (Continued)

56150000000.	9.2502	12.2157
56187500000.	9.1991	12.1920
56225000000.	9.1635	12.1817
56262500000.	9.1150	12.1720
56300000000.	9.0761	12.2071
56337500000.	9.0692	12.2467
56375000000.	9.0667	12.2555
56412500000.	9.0558	12.2833
56450000000.	9.0197	12.3501
56487500000.	9.0770	12.3581
56525000000.	9.1031	12.3892
56562500000.	9.1449	12.3388
56600000000.	9.1859	12.3300
56637500000.	9.1975	12.2460
56675000000.	9.1997	12.2237
56712500000.	9.2147	12.1506
56750000000.	9.1931	12.0867
56787500000.	9.1681	12.0450
56825000000.	9.1314	11.9702
56862500000.	9.0787	11.9380
56900000000.	9.0421	11.9022
56937500000.	9.0257	11.9065
56975000000.	8.9446	11.9349
57012500000.	8.8959	11.9564
57050000000.	8.8865	11.9422
57087500000.	8.8866	12.0007
57125000000.	8.8612	12.0387
57162500000.	8.8668	12.0574
57200000000.	8.8911	12.0824
57237500000.	8.9164	12.0747
57275000000.	8.9241	12.0873
57312500000.	8.9438	12.0156
57350000000.	8.9672	11.9597
57387500000.	8.9647	11.9380
57425000000.	8.9802	11.8461
57462500000.	8.9499	11.8129
57500000000.	8.9561	11.7306
57537500000.	8.8834	11.6747
57575000000.	8.8807	11.6243
57612500000.	8.8246	11.6171
57650000000.	8.7720	11.6046
57687500000.	8.7266	11.6254

Appendix D (Continued)

57725000000.	8.6944	11.6390
57762500000.	8.6835	11.6411
57800000000.	8.6632	11.6846
57837500000.	8.6584	11.7341
57875000000.	8.6455	11.7503
57912500000.	8.6559	11.7969
57950000000.	8.7234	11.7826
57987500000.	8.7436	11.7734
58025000000.	8.7712	11.7679
58062500000.	8.8040	11.6941
58100000000.	8.8180	11.6566
58137500000.	8.8118	11.5713
58175000000.	8.8182	11.5053
58212500000.	8.8137	11.4432
58250000000.	8.7751	11.3676
58287500000.	8.7410	11.3122
58325000000.	8.6857	11.3033
58362500000.	8.6455	11.2688
58400000000.	8.5892	11.2985
58437500000.	8.5628	11.3274
58475000000.	8.5088	11.3433
58512500000.	8.5173	11.3822
58550000000.	8.4971	11.4292
58587500000.	8.4948	11.4728
58625000000.	8.5157	11.4966
58662500000.	8.5457	11.5186
58700000000.	8.5806	11.5091
58737500000.	8.6133	11.4728
58775000000.	8.6443	11.4270
58812500000.	8.6975	11.3614
58850000000.	8.7205	11.3191
58887500000.	8.7095	11.2097
58925000000.	8.7076	11.1477
58962500000.	8.6812	11.0362
59000000000.	8.6255	10.9938
59037500000.	8.6201	10.9572
59075000000.	8.5679	10.9616
59112500000.	8.5341	10.9705
59150000000.	8.4924	11.0054
59187500000.	8.4456	11.0131
59225000000.	8.4719	11.0991
59262500000.	8.3788	11.1206

Appendix D (Continued)

59300000000.	8.3941	11.1535
59337500000.	8.4401	11.2249
59375000000.	8.5766	11.3206
59412500000.	8.6578	11.3342
59450000000.	8.7265	11.3293
59487500000.	8.6328	11.1524
59525000000.	8.7325	11.0817
59562500000.	8.9400	11.1464
59600000000.	8.8836	10.9472
59637500000.	8.7806	10.7247
59675000000.	8.7976	10.6837
59712500000.	8.7355	10.5843
59750000000.	8.8008	10.6180
59787500000.	8.6949	10.5770
59825000000.	8.5812	10.5265
59862500000.	8.4377	10.5235
59900000000.	8.3901	10.5779
59937500000.	8.3629	10.6909
59975000000.	8.3890	10.8174
60012500000.	8.3419	10.8933
60050000000.	8.3907	10.9873
60087500000.	8.4468	11.0778
60125000000.	8.4532	11.0615
60162500000.	8.5605	11.0885
60200000000.	8.6765	11.0414
60237500000.	8.8021	10.9490
60275000000.	8.9443	10.8708
60312500000.	8.9937	10.6536
60350000000.	9.0164	10.4907
60387500000.	9.0499	10.2788
60425000000.	8.8499	10.0219
60462500000.	8.7468	9.9075
60500000000.	8.7184	9.8811
60537500000.	8.5360	9.8705
60575000000.	8.4267	9.9336
60612500000.	8.2861	10.0102
60650000000.	8.1297	10.1199
60687500000.	8.0500	10.2722
60725000000.	7.9747	10.4238
60762500000.	7.9224	10.5674
60800000000.	7.9173	10.7124
60837500000.	7.9971	10.8317

Appendix D (Continued)

60875000000.	8.1242	10.9273
60912500000.	8.3517	10.9726
60950000000.	8.6543	10.9919
60987500000.	9.0557	10.9146
61025000000.	9.4977	10.7649
61062500000.	9.9459	10.5828
61100000000.	10.3479	10.3125
61137500000.	10.5748	10.0513
61175000000.	10.6035	9.7916
61212500000.	10.4375	9.6223
61250000000.	10.1604	9.5248
61287500000.	9.8092	9.4913
61325000000.	9.3508	9.5308
61362500000.	8.9205	9.6081
61400000000.	8.4888	9.7089
61437500000.	8.1142	9.8007
61475000000.	7.7830	9.9416
61512500000.	7.5323	10.0728
61550000000.	7.3141	10.2455
61587500000.	7.1383	10.4720
61625000000.	6.9992	10.7576
61662500000.	6.8474	11.0620
61700000000.	6.7407	11.3883
61737500000.	6.6451	11.7072
61775000000.	6.6329	12.0426
61812500000.	6.6705	12.3232
61850000000.	6.8208	12.5333
61887500000.	7.0160	12.6430
61925000000.	7.3099	12.6675
61962500000.	7.5758	12.5267
62000000000.	7.8359	12.2650
62037500000.	8.0345	11.8713
62075000000.	8.1837	11.3800
62112500000.	8.2154	10.9299
62150000000.	8.1585	10.4840
62187500000.	8.0651	10.1337
62225000000.	7.9291	9.8478
62262500000.	7.7704	9.6515
62300000000.	7.6020	9.5459
62337500000.	7.4181	9.4721
62375000000.	7.2689	9.4493
62412500000.	7.0895	9.4584

Appendix D (Continued)

62450000000.	6.9161	9.5175
62487500000.	6.7567	9.5759
62525000000.	6.5994	9.6655
62562500000.	6.4628	9.7749
62600000000.	6.3516	9.8753
62637500000.	6.3060	9.9795
62675000000.	6.3174	10.0584
62712500000.	6.4317	10.1328
62750000000.	6.5979	10.1422
62787500000.	6.8068	10.1393
62825000000.	7.0317	10.0714
62862500000.	7.2296	9.9720
62900000000.	7.4055	9.8379
62937500000.	7.5203	9.7048
62975000000.	7.5756	9.5887
63012500000.	7.6010	9.4738
63050000000.	7.5838	9.3879
63087500000.	7.5291	9.3129
63125000000.	7.4596	9.2600
63162500000.	7.3945	9.2017
63200000000.	7.3023	9.1841
63237500000.	7.2087	9.1773
63275000000.	7.1246	9.1328
63312500000.	7.1113	9.1084
63350000000.	7.0960	9.0736
63387500000.	7.0897	9.1816
63425000000.	7.0881	9.1655
63462500000.	7.1197	9.2041
63500000000.	7.2042	9.1958
63537500000.	7.2488	9.2734
63575000000.	7.3112	9.2805
63612500000.	7.3819	9.2026
63650000000.	7.4549	9.2965
63687500000.	7.4760	9.2332
63725000000.	7.5233	9.2886
63762500000.	7.4601	9.1917
63800000000.	7.5538	9.1391
63837500000.	7.4036	9.1621
63875000000.	7.3953	9.0358
63912500000.	7.4050	9.0025
63950000000.	7.2958	9.0263
63987500000.	7.3569	8.9422

Appendix D (Continued)

64025000000.	7.3726	8.9513
64062500000.	7.2847	9.0979
64100000000.	7.2496	8.9563
64137500000.	7.2551	8.9636
64175000000.	7.3347	9.0398
64212500000.	7.2506	9.0085
64250000000.	7.2971	8.9862
64287500000.	7.3777	8.9770
64325000000.	7.4353	9.1488
64362500000.	7.3472	9.0637
64400000000.	7.4073	9.0207
64437500000.	7.5685	8.9949
64475000000.	7.4689	9.0521
64512500000.	7.3550	8.9120
64550000000.	7.3411	8.8073
64587500000.	7.4043	8.8358
64625000000.	7.3949	8.8405
64662500000.	7.1715	8.8071
64700000000.	7.1304	8.6641
64737500000.	7.3018	8.6971
64775000000.	7.2653	8.7101
64812500000.	7.0661	8.8214
64850000000.	7.0878	8.6595
64887500000.	7.2546	8.7140
64925000000.	7.1866	8.7455
64962500000.	7.2286	8.8573
65000000000.	7.0752	8.7682

Appendix E Agilent 37397 Vector Network Analyzer Specifications

37X97D (40 MHz – 65 GHz)

Model	Frequency (GHz)	Port 1 Power, Typical		Noise Floor at Port 2 (dBm)[5]		System Dynamic Range	
			With Option 15		With Option 15		With Option 15
37397D	0.04	10	10	–88	–88	98	98
	2	5	5	–110	–110	115	115
	20	2	1	–106	–105	108	106
	40	1	0	–98	–97	99	97
	50	–1	–3	–94	–93	93	90
	65	–2	–4	–82	–80	80	76
37297D	0.04	10	10	–88	–88	98	98
	2	5	5	–110	–110	115	115
	20	1	0	–107	–106	108	106
	40	1	0	–100	–99	101	99
	50	–1	–3	–96	–95	95	92
	65	–1	–3	–84	–82	83	79

Test Port Characteristics[6]

Connector	Frequency[4] (GHz)	Directivity (dB)	Source Match (dB)	Load Match (dB)	Reflection Tracking (dB)	Transmission Tracking (dB)	Isolation (dB)
K (2.92 mm)	0.04	>40	>36	>40	±0.050	±0.050	>115
	2	>40	>36	>40	±0.050	±0.050	>115
	20	>40	>36	>40	±0.060	±0.070	>110
	40	>36	>32	>36	±0.060	±0.080	>100
	50	>34	>30	>34	±0.080	±0.100	>90
	65	>34	>28	>34	±0.100	±0.120	>80

4: Specifications between the stated frequencies are to be linearly interpolated as typical values.
5: RMS Value, 32 readings, CW – compensated for loss in available source power from test port cable connected between Port 1 and Port 2.
6: The specifications for Test Port Characteristics apply when the VNA Universal Test Port Adapters are connected, with or without phase equal insertables, to the test set ports and calibrated with the appropriate calibration kit at 23°C ±3°C using the SOLT calibration method with a sliding load to achieve 12-term error correction. (90 min. warm-up time is recommended.)

Signal Source Specifications

Resolution: 1 Hz

Frequency Stability:

Temperature: < 5×10^{-9} over 0°C to 55°C range
Aging: <1 x 10^{-9}/day

Source Power Level: The source power (dBm) may be set from the front panel menu or via GPIB. In addition, on 37300D models, the port 1 power may be attenuated in 10 dB steps, using the internal 70 dB (60 dB for 37397D) step attenuator. Similarly, high input signals into port 2, not exceeding 1 watt, can be attenuated up to 40 dB, using the internal port 2 step attenuator.

Sweep Type: Linear, CW, Marker, or N-Discrete point sweep

Phase Noise: >60 dBc/Hz at 10 kHz offset and 20 GHz center frequency

Spurious Response (Harmonics)

Frequency	Typical (at default power)
40 MHz to 20 GHz	<–40 dBc
20 GHz to 40 GHz	<–20 dBc
40 GHz to 65 GHz	<–20 dBc

Spurious Response (Non-harmonics): <–35 dBc at maximum rated power

High Level Noise (pk – pk typical at 1 kHz I.F. BW)

Frequency	Magnitdude (dB)	Phase (degrees)
40 MHz to 20 GHz	<0.04	<0.5
20 GHz to 40 GHz	<0.08	<1.0
40 GHz to 65 GHz	<0.25	<2.5

Receiver Noise Floor and System Dynamic Range into Direct Access Ports (Option 15 only)

Model	Frequency (GHz)	Typical Noise Floor* (dBm)	Power into b1 or b2 Ports at 0.2 dB Compression (dBm)	Typical System Dynamic Range (dB)
372xxD	0.04	–130	–12	>118
	2	–123	–10	>113
	20	–121	–7	>114
	40	–111	–8	>103
	50	–102	–3	>99
	65	–92	–3	>89
373xxD	0.04	–130	–12	>118
	2	–123	–9	>114
	20	–120	–6	>114
	40	–110	–6	>104
	50	–100	0	>100
	65	–90	0	>90

*RMS value, 10 Hz IF BW, 512 avg, 32 readings, CW

Power Flatness

Frequency	Flatness (dB)
40 MHz to 13.5 GHz	±1.5
13.5 GHz to 20 GHz	±2.0
20 GHz to 40 GHz	±3.0
40 GHz to 65 GHz	±5.0

Appendix F MathCAD Code for Planar Biological Structure

COHERENT MULTI-LAYER CALCULATOR

(Layer 3 is atmosphere, layer 2 is dry skin, layer 1 is infiltrated fat, layer 0 is organ.)

$f := 1.4 \cdot 10^9$ For reference only - not used in calculations

$B := 27 \cdot 10^6$ Bandwidth in Hertz

$\varepsilon 2prime := 39.661173$

$\varepsilon 2doubleprime := 13.300211$ Dry skin complex permittivity at frequency f

$\varepsilon 2 := \varepsilon 2prime - j \cdot \varepsilon 2doubleprime$

$\varepsilon 1prime := 11.15166$

$\varepsilon 1doubleprime := 1.9237886$ Fat layer complex permittivity at frequency f

$\varepsilon 1 := \varepsilon 1prime - j \cdot \varepsilon 1doubleprime$

$\alpha 2 := 0.2655$

$\beta 2 := 0.1872977$

$\gamma 2 := \alpha 2 + j \cdot \beta 2$ Dry skin propagation, dB per mm and radians per mm at frequency f

$\alpha 1 := 0.0731$

$\beta 1 := 0.098345573$

$\gamma 1 := \alpha 1 + j \cdot \beta 1$ Fat layer propagation, dB per mm and radians per mm at frequency f

$Temp2 := 300$ Dry skin temperature (300K = 80F)

$Temp1 := 310.2$ Fat layer temperature (310.2K = 98.6F)

$Temp0 := 310, 310.2 .. 313$ Organ temperature (98.3F to 103.7F)

$TempR := 300$ Radiometer antenna noise temperature

$L2 := 1$ Thickness of skin layer in mm

$L1 := 25$ Thickness of fat layer in mm

$Z3 := 376.73$ Free-space impedance (layer 3 is free space)

$Z2 := \frac{Z3}{\sqrt{\varepsilon 2}}$ Dry skin impedance

$Z1 := \frac{Z3}{\sqrt{\varepsilon 1}}$ Fat impedance

$\Gamma 12 := \frac{(Z2 - Z1)}{(Z2 + Z1)}$ Reflectance, fat-to-skin

$\Gamma 23 := \frac{(Z3 - Z2)}{(Z3 + Z2)}$ Reflectance, skin-to-air

$\Gamma 32 := -\Gamma 23$ Reflectance, air-to-skin

$k := 1.380650310^{-23}$ Boltzmann's Constant

$TR := k \cdot TempR \cdot B$

$T2 := k \cdot Temp2 \cdot B$ Convert temperatures into power levels

$T1 := k \cdot Temp1 \cdot B$

$T0(Temp0) := k \cdot Temp0 \cdot B$

Calculate effects of
attenuation and reflection

$$T0prime(Temp0) := T0(Temp0) \cdot \left[10^{\frac{-(\alpha 1 \cdot L1)}{10}}\right] \cdot \left[1 - \left(|\Gamma 12|\right)^2\right] + T1 - T1 \cdot \left[10^{\frac{-(\alpha 1 \cdot L1)}{10}}\right] \cdot \left[1 - \left(|\Gamma 12|\right)^2\right]$$

$$TE(Temp0) := T0prime(Temp0) \cdot \left[10^{\frac{-(\alpha 2 \cdot L2)}{10}}\right] \cdot \left[1 - \left(|\Gamma 23|\right)^2\right] + T2 - T2 \cdot \left[10^{\frac{-(\alpha 2 \cdot L2)}{10}}\right] \cdot \left[1 - \left(|\Gamma 23|\right)^2\right]$$

$$Tmeas(Temp0) := |TE(Temp0)| \cdot \left[1 - \left(|\Gamma 23|\right)^2\right] + TR \cdot \left(|\Gamma 32|\right)^2$$

$TempEmitted(Temp0) := \left|\frac{Tmeas(Temp0)}{k \cdot B}\right|$ Convert power level back to temperature

$TempF(Temp0) := \left(\frac{9}{5}\right) \cdot Temp0 - 459.666$

About the Author

Thomas Armand Ricard began his engineering education at Waterbury (CT) State Technical College (now part of Naugatuck Valley Community College), where he earned his ASEE degree with high honors in 1982. He completed his undergraduate studies at the University of Hartford, receiving his BSEE degree *cum laude* with mathematics minor in 1988. His graduate work began at Syracuse University as part of the General Electric Edison Engineering Program, where he earned his MSEE degree in 1991. After devoting his efforts to industry for more than a decade, he returned to academia and completed his doctoral requirements at the University of South Florida in 2008.

Mr. Ricard is a member of Phi Kappa Phi, Tau Beta Pi and Eta Kappa Nu honor societies and is a biographee in several Marquis Who's Who publications. He lives in Tampa Florida with his wife Gina and their daughters, Bernadette and Amanda.